energies

MDPI

Article

Loss Model Control for Efficiency Optimization and Advanced Sliding Mode Controllers with Chattering Attenuation for Five-Phase Induction Motor Drive

Hassen Moussa [1], Saber Krim [1], Hichem Kesraoui [1], Majdi Mansouri [2,*] and Mohamed Faouzi Mimouni [1]

[1] Laboratory of Automatic, Electrical Systems and Environment (LASEE), National Engineering School of Monastir, University of Monastir, Monastir 5019, Tunisia; hassen.moussa@mahdia.r-iset.tn (H.M.); saber.krim@issatkas.kairouan.tn (S.K.); hichem.kesraoui@mahdia.r-iset.tn (H.K.); mfaouzi.mimouni@enim.rnu.tn (M.F.M.)

[2] Electrical and Computer Engineering Program, Texas A&M University at Qatar, Doha 23874, Qatar

* Correspondence: majdi.mansouri@qatar.tamu.edu

Abstract: This paper proposes firstly a Second Order Sliding Mode Control (SOSMC) based on a Super Twisting Algorithm (STA) (SOSMC-STA) combined with a Direct Field-Oriented Control (DFOC) strategy of a Five-Phase Induction Motor (FPIM). The SOSMC-STA is suggested for overcoming the shortcomings of the Proportional Integral Controller (PIC) and the Conventional Sliding Mode Controller (CSMC). Indeed, the main limitations of the PIC are the slower speed response, the tuning difficulty of its parameters, and the sensitivity to changes in system parameters, including variations in process dynamics, load changes, or changes in setpoint. It is also limited to linear systems. Regarding the CSMC technique, its limitation is the chattering phenomenon, characterized by the rapid switching of the control signal. This phenomenon includes high-frequency oscillations which induce wear and tear on mechanical systems, adversely affecting performance. Secondly, this paper also proposes a Loss Model Controller (LMC) for FPIM energy optimization. Thus, the suggested LMC chooses the optimal flux magnitude required by the FPIM for each applied load torque, which consequently reduces the losses and the FPIM efficiency. The performance of the optimized DFOC-SOSMC-STA based on the LMC is verified using numerical simulation under the Matlab environment. The analysis of the simulation results shows that the DFOC-SOSMC-STA guarantees a high dynamic response, chattering reduction, good precision, and robustness in case of external load or parameter disturbances. Moreover, the DFOC-SOSMC-STA, combined with the LMC, reduces losses and increases efficiency.

Keywords: five-phase induction motor; sliding mode control; chattering attenuation; direct field-oriented control; loss model control

Citation: Moussa, H.; Krim, S.; Kesraoui, H.; Mansouri, M.; Mimouni, M.F. Loss Model Control for Efficiency Optimization and Advanced Sliding Mode Controllers with Chattering Attenuation for Five-Phase Induction Motor Drive. *Energies* **2024**, *17*, 4192. https://doi.org/10.3390/en17164192

Academic Editor: Gianluca Brando

Received: 4 December 2023
Revised: 28 January 2024
Accepted: 2 February 2024
Published: 22 August 2024

1. Introduction

In recent years, there has been an increasing interest in using multiphase Induction Motors (IMs) in various industrial applications. Multiphase motors can have several advantages over traditional three-phase motors, including improved performance and efficiency [1]. Multiphase motors can operate with more than three phases, typically ranging from five to nine phases [2,3]. The increased number of phases results in a more sinusoidal current waveform, which reduces the losses caused by higher current harmonics [3]. Additionally, the increased number of phases can reduce the magnitude of the electromagnetic torque ripple, resulting in smoother operations and less mechanical stress on the motor [4]. Furthermore, multiphase motors can provide improved reliability and fault tolerance compared to three-phase motors [5]. If one phase fails in a three-phase motor, the motor will cease to function. However, in a multiphase motor, the remaining phases can compensate for the lost phase, allowing the motor to continue to operate at a

reduced level of performance. Multiphase motors have been applied in various industries, including electric traction, aviation, and ship propulsion. In these industries, the improved performance and efficiency of multiphase motors can provide significant benefits, such as reduced energy consumption and increased reliability [1–6].

It should be noted that the control of Five-Phase Induction Motors (FPIMs) holds immense significance in various industrial applications. Unlike traditional three-phase motors, FPIMs offer superior performance, efficiency, and reliability. Precise control of these motors allows for smoother operations, reduced vibrations, and enhanced torque production, making them ideal for demanding tasks, such as robotics, electric vehicles, and aerospace applications. Thus, the two most widely recognized and used control strategies for motors, especially for Five-Phase Induction Motors (FPIM), are Direct Field-Oriented Control (DFOC) [7] and Direct Torque Control (DTC) [8]. In fact, DFOC is based on a rotor flux regulation loop and internal current control loops to achieve an independent regulation of the flux level and the load current component that describes the electromagnetic torque. The DTC enables direct control of the machine's torque and flux levels by eliminating current control loops and using hysteresis controllers. Both control structures have advantages and disadvantages, extensively discussed in various publications [9], with one group of scientists supporting DFOC and another group of scientists supporting DTC. In modern industrial control applications, control structures must meet all requirements in terms of complexity, parameter sensitivity, dynamic performance, and cost. Ultimately, the choice between DFOC and DTC depends on the specific application requirements, as well as the cost and design complexities associated with each technique. DTC exhibits significant ripples in the electromagnetic torque and stator flux, remarkable distortions in the stator current, and variations in the switching frequency, which causes mechanical vibrations and switching losses, leading to premature ageing of the system [10,11]. On the other hand, DFOC offers good performance in terms of accuracy, reduced ripples and distortions, and constant switching frequency [12].

The classical DFOC strategy includes control loops based on Proportional-Integral Controllers (PICs) for controlling the rotor speed, the rotor flux, and the direct/quadratic current components. The gain values of these controllers are typically obtained through an analytical method based on a simplified linear IM model. Furthermore, these gain values are closely related to the IM parameters. Consequently, PICs exhibit limited performance in the presence of disturbances, uncertainties, and variations in IM parameters. Additionally, the system dynamics and stability are affected [13]. To address the constraints of the mentioned approach and achieve improved control performance in the face of uncertainties and external disturbances, robust nonlinear control techniques, modified linear control techniques, and intelligent control methods have been developed for IM control and other industrial systems. These methods include cascaded control [6], input-output feedback linearization [14], Modified Linear Technique [15], Bat algorithm based control and modified bat algorithm based control [16], Error Feedback Fuzzy Model [17], fuzzy logic control [18,19], predictive control [20,21], and Sliding Mode Control (SMC) [5,14,22–25], among others like exact tracking error dynamics passive output feedback (ETEDPOF) methodology [26] and robust adaptive control [27]. Certainly, as outlined in [27], the authors devised a PD controller incorporating a neural network-based cascade scheme to effectively handle the compensation of uncertainties in a robot manipulator.

In the same context, and relative to the other control techniques, the SMC offers distinct advantages relative to other control strategies in various engineering applications. One of its primary benefits is its robustness in the face of uncertainties and external disturbances. The SMC excels at maintaining system stability and performance, even when confronted with unpredictable variations or disturbances, making it particularly suitable for complex and dynamic systems. Another key advantage of SMC is its ability to handle nonlinear systems effectively. Unlike linear control strategies that may struggle with nonlinearities, SMC can be designed to accommodate and control such systems, providing precise and reliable performance. Furthermore, SMC can offer faster transient responses, reduced

settling times, and improved tracking accuracy compared to some traditional control methods [28]. Therefore, the use of the DFOC strategy with Conventional Sliding Mode Controllers (CSMCs) offers good performance compared to DFOC-PICs and is characterized by its simplicity in design and implementation. The combination of DFOC and CSMCs (DFOC-CSMCs) is an effective control method due to its superior robustness against model uncertainties, parameter variations, and external disturbances [29,30]. It is worth noting that the main drawback of DFOC-SMCs is the undesirable effect known as "chattering". This phenomenon includes high-frequency oscillations that lead to dynamic instability of the system. Relatively speaking, several studies on CSMCs have focused on reducing chattering [31–33]. The solutions developed in these studies to mitigate the chattering phenomenon are as follows:

- Replacing discontinuous control functions with "saturation" or "sigmoid" functions is a common approach used in SMC to achieve continuous control and reduce vibrations. However, one of the main drawbacks of this approach is that the system state trajectory does not converge exactly towards the sliding surface but wraps around it, which can reduce the system's accuracy and robustness to disturbances [34–36].
- A controller with a dynamic gain can be a useful tool in situations where there are uncertainties or disturbances in the system being controlled. Adaptive SMC, which adjusts the gain based on the level of uncertainties or disturbances, can be particularly effective in reducing chattering. In [37], adaptive SMC with first-order adaptation is proposed for the control of electropneumatic actuators. The controller used an adaptive gain that was updated online based on the system output error and its time derivative. The controller was evaluated with simulation studies and showed improved performance compared to fixed-gain SMC. In [38], robust adaptive SMC was put forward for Takagi-Sugeno fuzzy systems. The controller used a dynamic gain that was updated online based on a measure of the uncertainty in the system. The controller was suggested to provide improved tracking performance and robustness to uncertainties in the system. Overall, adaptive SMC with a dynamic gain can be an effective tool for controlling systems with uncertainties or disturbances. By adjusting the gain based on the uncertainty level, these controllers can provide improved performance and reduced chattering compared to fixed-gain controllers.
- Several researchers have also advocated the use of fractional-order SMC to overcome the limitations of CSMC. In contrast to CSMC, fractional-order SMC incorporates a fractional-order term in the sliding surface [39]. This fundamental operation of fractional calculus involves performing differentiations and integrations with fractional exponents, necessitating digital circuits with higher computational power.
- Fractional-order SMC has certain limitations, particularly concerning the consideration of uncertainties and sensitivity to noise, which pose challenges in its design and implementation. To address these limitations, researchers have explored approaches to make fractional-order SMC more robust, including fuzzy logic techniques and neural networks, to adjust the controller parameters based on changing system conditions. This enhances performance and reduces sensitivity to disturbances and uncertainties [40–42]. Nonetheless, fractional-order SMCs have shown promising results in controlling nonlinear systems [43–45]. The combination of fractional-order sliding mode control and intelligent techniques can improve robustness and reduce vibrations, but it also increases the complexity of the implemented algorithms, requiring digital circuits with higher computational power.
- The sliding surface is a key component in SMC that helps to drive the system towards a desired state or trajectory. The addition of integral parts to the sliding surface is a modification that can improve the performance of the controller. This modification aims to address the issue of chattering, which is a common problem in SMC [22,23].
- In their research [46], the authors introduced a high-gain approach to mitigate position or velocity perturbations in inverted pendulums. This method, in contrast to a sliding mode control technique, produced a control signal without inducing chattering.

- In their work, [46,47] introduced higher-order SMCs. The latter generalized first-order control by utilizing higher-order derivatives of the sliding surface (S) instead of restricting itself to just the first derivative. However, to implement such a controller, derivatives of the sliding variable were necessary, making this approach more demanding in terms of the required information for its design. An outstanding exception was the super-twisting sliding mode algorithm, which only requires the measurement of the sliding variable. This method is highly powerful and therefore very appealing for controlling three-phase induction motors and other applications, as was demonstrated in [14,48–51]. Currently, the latest control technique has been proposed by a few researchers for controlling the FPIM. Unfortunately, its performance has not been detailed in [52,53]. In their investigation [46], the authors used a Direct Field-Oriented Control (DFOC) method employing a second order Supertwisting Algorithm (STA) for a five-phase squirrel-cage induction motor. Although the supertwisting algorithm was proposed to enhance control loops for rotor speed, rotor flux, and currents, the study falls short in providing a thorough examination of the control system's performance. Notably, aspects such as robustness under load torque disturbances, variations in rotor resistance, and the Total Harmonic Distortion (THD) of the stator current, especially at low speeds, have not been extensively discussed. In another related study [53], the authors presented an enhanced field-oriented control of FPIM using an STA exclusively for inner current control loops. Unfortunately, simulation studies in this work lack comprehensive details, as the authors only presented a scenario in steady-state operation without a load.

In this work, we attempt to develop and apply Second Order Sliding Mode Controllers (SOSMCs) based on the Super Twisting Algorithm (STA) (SOSMC-STAs) based DFOC for an FPIM with a highly detailed performance analysis based on multiple evaluation scenarios in steady state and at low-speed ranges, under sudden load torque application and rotor resistance variations. The proposed SOSMC-STA performance will be analyzed using other criteria, such as the Integral of Absolute Error (IAE), the Integral of Squared Error (ISE), the Integral of Time multiplied by Absolute Error (ITAE), and the Total Harmonic Distortion (THD). This comprehensive study distinguishes itself from previously published research works and will present valuable results that are particularly beneficial for designers of variable-speed drives. The proposed SOSMC-STAs controllers are combined with the DFOC strategy, which will be denoted by DFOC-SOSMC-STAs in the rest of the paper. Furthermore, in our work, the suggested DFOC-SOSMC-STAs are compared with classical DFOC based on PICs (DFOC-PICs), classical DFOC based on Integral-Proportional Controllers (DFOC-IPCs), and DFOC based on CSMCs (DFOC-CSMCs). The comparison results show that the proposed DFOC-SOSMC-STAs reduce chattering, increase speed and precision, enhance the control system robustness against variations in FPIM parameters and load disturbances, and stand out for their remarkable simplicity in terms of design and implementation.

Recently, electric motors have been estimated to consume a significant portion of the world's electricity. According to data from the International Energy Agency (IEA), electric motors account for approximately 45–50% of global electricity consumption in the industrial and commercial sectors combined. This includes both low-power motors found in appliances and high-power motors used in heavy industrial applications. In this context, several researchers have proposed various approaches to improve the energy efficiency of IMs by selecting the optimal reference flux for each load. These approaches can be categorized into two main categories: the Search Controller (SC) [54–59], and the Loss Model Controller (LMC) [49,59]. Indeed, the Search Controller (SC) relies on measuring the Input power or the DC bus power and applying artificial intelligence (fuzzy logic, neural networks, P&O, etc.) to find the rotor flux reference that results in minimum power for a given load. The SC method is insensitive to motor parameters, but it requires additional hardware to measure the DC bus current. The main drawbacks of the search-based control SC are slow convergence and torque ripples [57,59]. The LMC is based on the steady-state

model of the IM, expressed in the rotor flux orientation reference frame, to select the optimal rotor flux reference that will be online-tuned to optimize the IM efficiency. This rotor flux reference is determined based on the calculation of minimum IM losses. The LMC method has the advantage of being simple and fast. However, its accuracy depends on correct motor modeling and loss estimation. Adding the LMC to DFOC is one of the control strategies aimed at energy savings. It is true that the LMC has been addressed in the literature for conventional structure machines like three-phase induction machines, but, unfortunately, it is not applied to five-phase induction machines. In this context, we have currently initiated the minimization of copper losses for the FPIM to determine the reference rotor flux for a given load torque profile. We have demonstrated that adjusting the rotor flux level in accordance with the load ensures better steady-state operation of the machine without significantly sacrificing the dynamics of the torque or speed response. In this context, we can identify the second significant contribution of this article which consists of applying the LMC to an FPIM.

Finally, our primary objectives and contributions to both theoretical and simulation studies can be summarized as follows:

(i) An updated vector control approach, employing the SOSMC-STAs for the FPIM, is presented. This novel control scheme offers several benefits, including enhanced system robustness against load disturbances and stator resistance variations, reduced chattering, rapid convergence with high precision, and minimized torque ripples. It is noteworthy that the existing literature primarily uses PI-based or SMC-based vector control for the FPIM without the STA.

(ii) LMC for FPIM loss minimization is put forward to calculate the optimal required rotor flux as a function of motor operation conditions, which consequently reduces the electrical energy consumption in steady-state operations and improves the FPIM efficiency. To the best of our knowledge, this marks the initial utilization of LMC in the literature in conjunction with DFOC-SOSMC-STAs to enhance the efficiency of the FPIM.

(iii) In simulation, the suggested vector control strategy, employing the STSMC-STAs, is developed within the Matlab/Simulink environment. The results demonstrate outstanding robustness in the face of load torque disturbances, stator resistance variations, and rapid dynamic responses with exceptional precision.

(iv) A comparative analysis involving various simulation scenarios is conducted to evaluate the performance of PICs, IPCs, CSMCs, and our proposed SOSMC-STAs. The results indicate that the suggested controller outperforms the others across multiple criteria, including speed response time, speed overshooting, robustness against load disturbances and parameter variations, chattering reduction, and torque ripple minimization. Moreover, the proposed LMC offers satisfactory performance in terms of efficiency optimization.

The structure of the remaining part of the article is as follows: Section 2 introduces the state model of the FPIM, while Section 3 presents the DFOC control strategy. Sections 4 and 5 are dedicated to synthesizing PI and IP controllers, respectively, for speed, rotor flux, as well as direct and quadrature stator currents. In Section 6, we develop CSMS and SOSSMC-STAs for speed, direct and quadrature stator currents, and rotor flux. Section 7 discusses the optimization strategy for FPIM efficiency based on the loss model. Simulation results, evaluating the performance of the proposed control strategy, are presented in Section 8. Finally, our conclusions are provided in Section 9.

2. Modeling of FPIM

The formulation of the FPIM in the rotating reference frame (d-q, x-y) yields the following electrical and mechanical equations [5,6,60]:

$$\begin{cases} \dot{i}_{sd} = \frac{K}{T_r}\psi_{rd} + K{\cdot}p{\cdot}\Omega{\cdot}\psi_{rq} - \gamma{\cdot}i_{sd} + \omega_s{\cdot}i_{sq} + \frac{v_{sd}}{\sigma L_s} \\ \dot{i}_{sq} = -K{\cdot}p{\cdot}\Omega{\cdot}\psi_{rd} + \frac{K}{T_r}\psi_{rq} - \gamma{\cdot}i_{sq} - \omega_s{\cdot}i_{sd} + \frac{v_{sq}}{\sigma L_s} \\ \dot{i}_{sx} = -\frac{R_s}{L_{ls}}i_{sx} + \frac{1}{L_{ls}}v_{sx} \\ \dot{i}_{sy} = -\frac{R_s}{L_{ls}}i_{sy} + \frac{1}{L_{ls}}v_{sy} \\ \dot{\psi}_{rd} = -\frac{1}{T_r}{\cdot}\psi_{rd} + \omega_r{\cdot}\psi_{rq} + \frac{L_m}{T_r}{\cdot}i_{sd} \\ \dot{\psi}_{rq} = -\omega_r{\cdot}\psi_{rd} - \frac{1}{T_r}{\cdot}\psi_{rq} + \frac{L_m}{T_r}{\cdot}i_{sq} \\ \dot{\omega} = \frac{p}{J}(T_e - T_l) - \frac{f}{J}\omega \end{cases} \quad (1)$$

In addition, the electromagnetic T_e torque and the mechanical equation of the FPIM can be determined by:

$$T_e = \frac{p{\cdot}M}{L_r}{\cdot}\left(\psi_{rd}{\cdot}i_{sq} - \psi_{rq}i_{sd}\right) \quad (2)$$

$$\dot{\Omega} = \frac{T_e}{J} - \frac{T_L}{J} - \frac{f}{J}{\cdot}\Omega \quad (3)$$

where:

- $\sigma = 1 - \frac{{L_m}^2}{L_s{\cdot}L_r}$, $K = \frac{1-\sigma}{L_m{\cdot}\sigma}$, $T_r = \frac{L_r}{R_r}$, $T_s = \frac{L_s}{R_s}$, $\gamma = \frac{1}{\sigma{\cdot}T_s} + \frac{1}{T_r}{\cdot}\frac{1-\sigma}{\sigma}$, $L_m = \frac{5}{2}M$
- i_{sd}, i_{sq}, i_{sx}, i_{sy}: *d*-*q*, *x*-*y*-axis stator current components,
- v_{sd}, v_{sq}, v_{sx}, v_{sy}: *d*-*q*, *x*-*y*-axis stator voltage components,
- ψ_{rd}, ψ_{rq}: *d*-*q*-axis rotor flux components,
- ω_s: synchronous angular speed,
- Ω: mechanical speed,
- ω: electrical motor speed ($\omega = p\Omega$),
- ω_r: slip angular speed ($\omega_s - \omega$),
- R_s, R_r: stator and rotor resistance,
- M: Maximum value of the stator to rotor mutual inductances in the phase.
- L_s, L_r: stator and rotor cyclic inductance,
- L_m: cyclic mutual inductance stator-rotor,
- L_{ls}: stator leakage inductance,
- T_r, T_s: stator and rotor time constant,
- σ: leakage coefficient,
- p: pole-pair number,
- J: rotor Inertia,
- f: viscous Friction coefficient.

3. Rotor Field Orientation Vector Control

The field-oriented control strategy was developed to control the electromagnetic torque in transient conditions. The concept of decoupling in vector control of alternating current machines emerged in the late 1960s. Initially, in 1969, Hasse introduced the method of indirect field-oriented control, followed by Blaschke in 1971 who developed a theory of control known as DFOC. These approaches have enabled the assimilation of the asynchronous machine with a separately excited direct current machine, where a natural decoupling exists between the flux and the electromagnetic torque. This is achieved by considering the orientation of the flux relative to the *d*-axis.

$$\begin{cases} \psi_{rd} = \psi_r \\ \psi_{rq} = 0 \end{cases} \quad (4)$$

Given that $\psi_{rq} = 0$ and $\psi_r = \psi_{rd}$, the set of FPIM equations presented in (1) and (2) will be as follows:

$$\begin{cases} \dot{i}_{sd} = \frac{K}{T_r}\psi_r - \gamma \cdot i_{sd} + \omega_s \cdot i_{sq} + \frac{v_{sd}}{\sigma L_s} \\ \dot{i}_{sq} = -K \cdot p \cdot \Omega \cdot \psi_r - \gamma \cdot i_{sq} - \omega_s \cdot i_{sd} + \frac{v_{sq}}{\sigma L_s} \\ \dot{i}_{sx} = -\frac{R_s}{L_{ls}} i_{sx} + \frac{1}{L_{ls}} v_{sx} \\ \dot{i}_{sy} = -\frac{R_s}{L_{ls}} i_{sy} + \frac{1}{L_{ls}} v_{sy} \\ \dot{\psi}_r = -\frac{1}{T_r} \cdot \psi_r + \frac{L_m}{T_r} \cdot i_{sd} \\ 0 = -\omega_r \cdot \psi_r + \frac{L_m}{T_r} \cdot i_{sq} \\ \dot{\omega} = \frac{p}{J}(T_e - T_l) - \frac{f}{J}\omega \end{cases} \tag{5}$$

$$T_e = P \cdot \frac{L_m}{L_r} \cdot (\psi_r \cdot i_{sq}) \tag{6}$$

Considering (5), the quantities ψ_r, ω_s and θ_s are given by the following equations:

$$\begin{cases} \psi_r = \frac{L_m}{1 + T_r \cdot s} i_{sd} \\ \omega_s = \frac{L_m}{\psi_r \cdot T_r} \cdot i_{sq} + p\Omega \\ \theta_s = \int (\omega_r + p \cdot \Omega) \cdot dt \end{cases} \tag{7}$$

where θ_s is the angle of the direct and inverse Park transformations. From (5), the direct and quadrature stator voltages are given by the following equations, respectively:

$$\begin{cases} v_{sd} = \sigma L_s \dot{i}_{sd} + \gamma \sigma L_s i_{sd} - \sigma L_s \frac{K}{T_r} \psi_r - \sigma L_s \omega_s i_{sq} \\ v_{sq} = \sigma L_s \dot{i}_{sq} + \gamma \sigma L_s i_{sq} + \sigma L_s K p \Omega \psi_r + \sigma L_s \omega_s i_{sd} \end{cases} \tag{8}$$

To ensure decoupling between the two axes (d, q) and to calculate the controller coefficients for the stator currents in a straightforward manner, we can rewrite the FPIM equations as follows:

$$\begin{cases} v_{sd} = v_d + e_d \\ v_{sq} = v_q + e_q \end{cases} \tag{9}$$

with:

$$\begin{cases} v_d = \sigma L_s \dot{i}_{sd} + \gamma \sigma L_s i_{sd} \\ v_q = \sigma L_s \dot{i}_{sq} + \gamma \sigma L_s i_{sq} \end{cases} \tag{10}$$

and

$$\begin{cases} e_d = -\sigma L_s \frac{K}{T_r} \psi_r - \sigma L_s \omega_s i_{sq} \\ e_q = \sigma L_s K p \Omega \psi_r + \sigma L_s \omega_s i_{sd} \end{cases} \tag{11}$$

e_d: d- back electromotive force.
e_q: q- back electromotive force.

The expressions for the direct and quadrature stator currents are given by the following equations, respectively. The direct stator current is given by:

$$i_{sd} = \frac{\frac{\gamma}{\sigma L_s}}{1 + \frac{1}{\gamma} s} \cdot v_d \tag{12}$$

The quadrature stator current is as follows:

$$i_{sq} = \frac{\frac{\gamma}{\sigma L_s}}{1 + \frac{1}{\gamma} s} \cdot v_q \tag{13}$$

Equations (6) and (7) show that the electromagnetic torque and the magnetic flux are individually regulated based on currents i_{sq} and i_{sd}. Thus, the decoupling between the torque and the flux is ensured by the independence between i_{sq} and i_{sd} according to (12) and (13).

Figure 1 represents the schematic of DFOC for the FPIM. The components of this control include the speed control loop, stator current control loops i_{sq}, i_{sd}, i_{sx} and i_{sy}, the rotor flux control loop ψ_r, the estimation block of θ_s, ω_r and ψ_r, the direct and inverse Park transformation blocks, and the decoupling calculation blocks e_d and e_q.

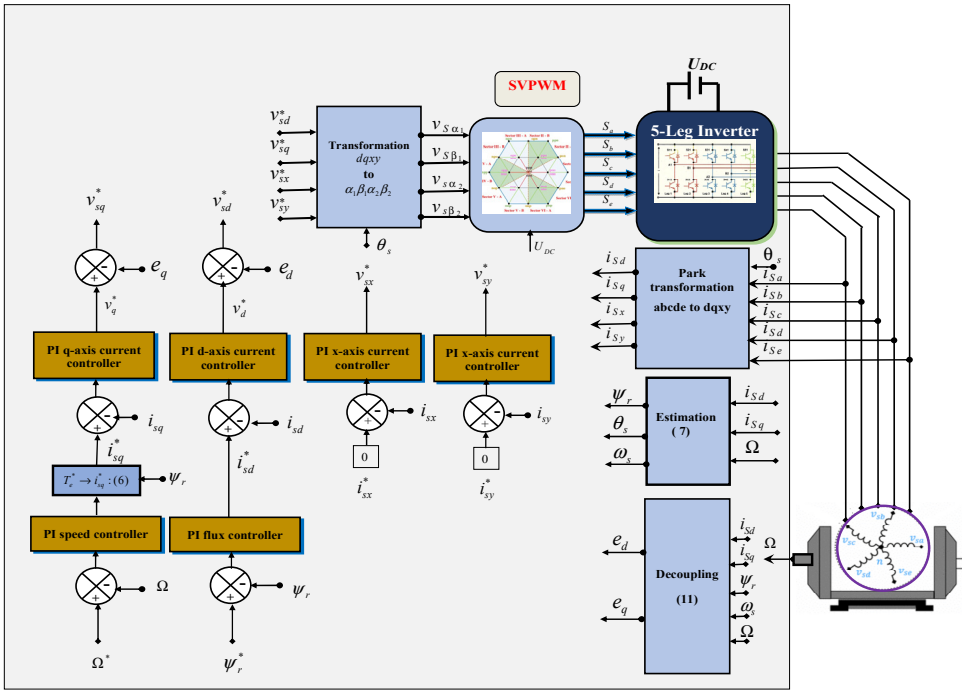

Figure 1. Structure of conventional DFOC strategy for FPIM based on PICs.

The speed is regulated by a proportional-integral controller (PIC), and the output of this controller represents the reference for the electromagnetic torque T_e^*. Equation (5) allows us to calculate the reference for the quadrature stator current i_{sq}^* for the inner current loop i_{sd}. Through a proportional-integral controller (PIC), the current controller i_{sd} provides the reference v_q^* that is added to e_q to construct the reference for the quadrature voltage v_{sq}^*.

In parallel with the speed loop, there is a rotor flux regulation loop Ψ_r cascaded with a direct stator current regulation loop i_{sd}. The rotor flux controller provides the reference for the stator current i_{sd}^*, and the current controller gives the reference v_q^*. This is added to e_d to form a reference for the stator voltage v_{sd}^*. The goal is to adjust this current i_{sd}^* to keep the rotor flux in phase with the d-axis reference.

Currents i_{sx} and i_{sy} are kept at zero since neither of them contributes to torque generation. The decoupling block calculates e_d to and e_q, which are essential for making the d and q axes completely independent.

The FPIM is powered by a five-leg inverter and is controlled using a Space Vector Pulse Width Modulation (SVPWM) technique employing four vectors per sector [61].

The conventional DFOC control strategy uses PICs for the different control loops, but it is not robust against parameter variations in the machine and against external disturbances. Particularly at low-speed ranges, it does not accurately track either speed or torque profiles. To overcome the latter control technique limitations, a hybrid control technique based on the combination between the DFOC strategy and SOSMCs based on STA (SOSMC-STAs) is proposed, and will be developed in the following sections [8,20].

4. Synthesis of PI Controller

4.1. Speed PI Controller

The block diagram of the closed-loop speed controller is depicted in Figure 2 [14,62]. The integral and proportional parameters of this controller are denoted as $K_{p\Omega}$ and $T_{i\Omega}$, respectively. Ω and Ω* represent the actual and reference rotor speeds, respectively. T_e^*

and T_l represent the reference and load torque, respectively. The adjustment of the speed controller parameters is carried out to achieve the desired performance of the closed-loop system by specifying the damping coefficient ξ, and the natural frequency w_0. Referring to Figure 2, the closed-loop transfer function $G_{cl}(s)$ can be expressed as follows:

$$G_{cl}(s) = \frac{T_{i\Omega}s + 1}{\frac{JT_{i\Omega}}{K_{p\Omega}}s^2 + T_{i\Omega}\left(1 + \frac{f}{K_{p\Omega}}\right)s + 1} \tag{14}$$

By identifying the denominator of $G_{cl}(s)$ into a canonical form $\frac{s^2}{w_0^2} + \frac{2\xi}{w_0}s + 1$, we obtain the following relationships:

$$\begin{cases} \frac{1}{w_0^2} = \frac{JT_{i\Omega}}{K_{p\Omega}} \\ \frac{2\xi}{w_0} = T_{i\Omega}\left(1 + \frac{f}{K_{p\Omega}}\right) \end{cases} \tag{15}$$

To achieve an overshoot-free response, the damping coefficient is set to ξ = 1, corresponding to the following relation: $w_0 \times tresp = 4.75$, as stated in Table A3 Here, tresp represents the speed response time.

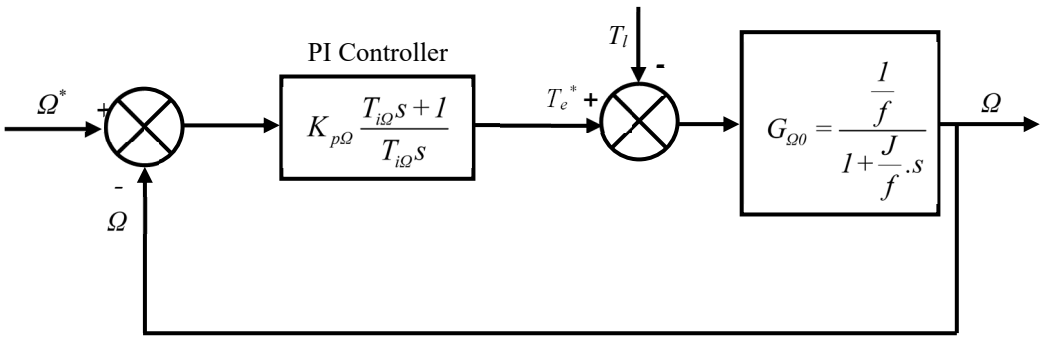

Figure 2. Block diagram of the closed-loop speed control.

4.2. Currents PI Controllers

The control loops for currents are established within the (*d*-*q*) and (*x*-*y*) frames. Fixed reference currents facilitate the utilization of PI controllers, simplifying and enhancing control efficiency. The parameters of the PI current controllers are determined by two criteria [62,63], which are:

(i) The zero point of the current controller nullifies the dominant time constant's pole in the process.

(ii) The feedback loop's time constant is deliberately set lower than that of the process.

The block diagram of the closed-loop for the d-q current controllers is depicted in Figure 3.

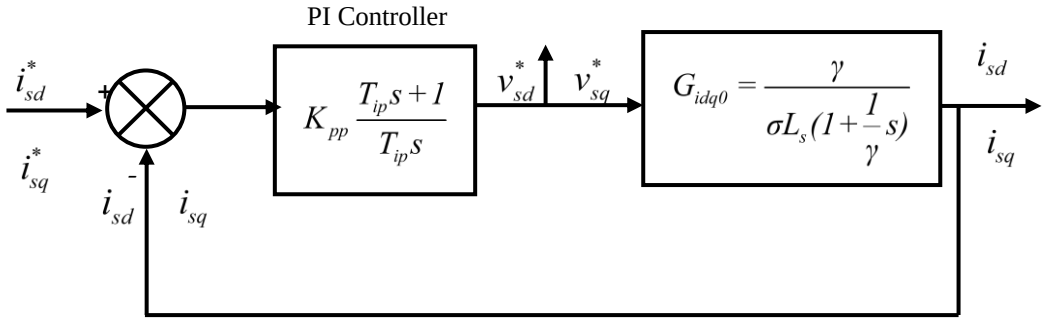

Figure 3. Block diagram of the closed-loop for the d-q current controllers.

The transfer function of the open loop along the *d-q* axis current is provided by:

$$G_{dqo}(s) = K_{pp}\frac{T_{ip}s+1}{T_{ip}s}\cdot\frac{1}{\sigma L_s\left(1+\frac{1}{\gamma}s\right)} \tag{16}$$

Considering the first rule:

$$T_{ip}s+1 = 1+\frac{1}{\gamma}s \tag{17}$$

Consequently, the simplified closed-loop transfer function is formulated as follows:

$$G_{dqc}(s) = \frac{1}{1+\frac{T_{ip}\sigma L_s}{K_{pp}\gamma}s} = \frac{1}{1+T_c s} \tag{18}$$

T_C is the time constant of the feedback loop of the *d-q* axis current loop is set at a fixed value according to [14,60,61].

$$T_C = \frac{T_{ip}\sigma L_s}{K_{pp}\gamma} \tag{19}$$

Therefore, the parameters for the *d-q* axis current controllers are as follows:

$$\begin{cases} T_{ip} = \frac{1}{\gamma} \\ K_{pp} = \frac{\sigma L_s}{0.116\gamma} \end{cases} \tag{20}$$

The block diagram of the closed-loop for the *x-y* current controllers is depicted in Figure 4.

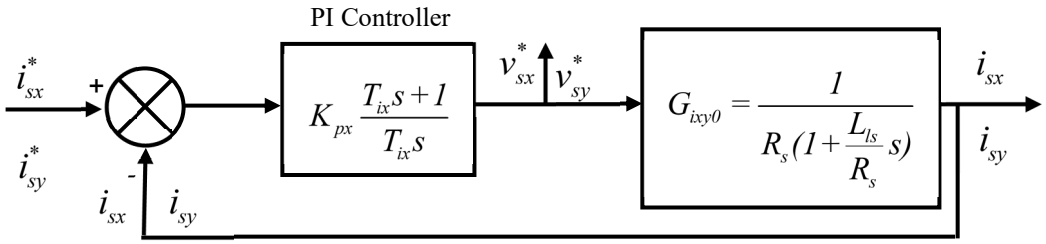

Figure 4. Block diagram of the closed-loop for the x-y current controllers.

The same method is applied to determine the parameters of the PI controllers for the *x-y* current components, resulting in:

$$\begin{cases} T_{ix} = \frac{L_{ls}}{R_s} \\ K_{px} = \frac{R_s}{0.116} \end{cases} \tag{21}$$

4.3. Flux PI Controller

Respecting the first and second synthesis rules for PI controllers from reference [62,63], the parameters of the flux controller in Figure 5 are selected by:

$$\begin{cases} T_{i\varphi_r} = T_r \\ K_{p\varphi_r} = \frac{1}{0.116\cdot L_m} \end{cases} \tag{22}$$

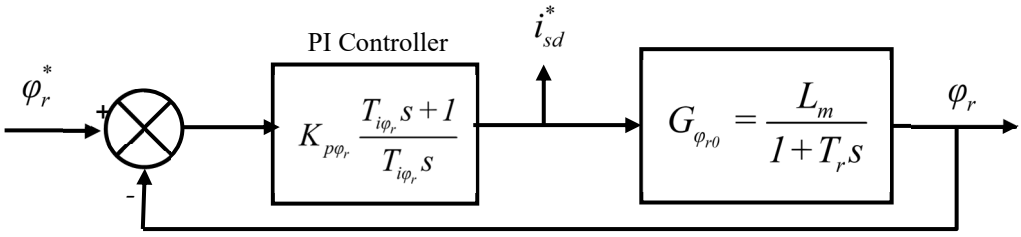

Figure 5. Block diagram of the closed loop for flux controller.

5. Synthesis of IP Controllers

The functional diagram presenting a system defined by its transfer function G(s) with the IP controller is depicted in Figure 6 [61].

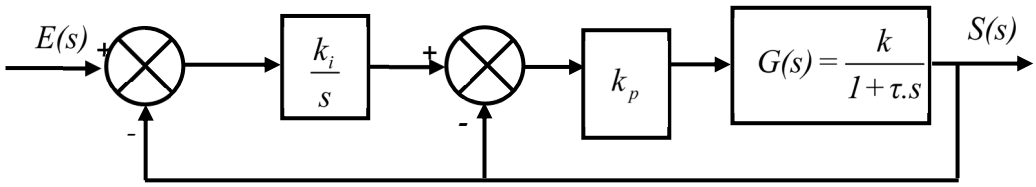

Figure 6. Structure with an IP controller.

Referring to references [14,63], the parameters k_i and k_p are given by the following expressions:

$$\begin{cases} k_i = \frac{94}{k} \\ k_p = \frac{24}{\tau} \end{cases} \quad (23)$$

According to (23), the parameters of the following controllers are defined:

5.1. Speed IP Controller

The speed controller parameters are given by (24):

$$\begin{cases} k_i = 94f \\ k_p = \frac{24}{J} f \end{cases} \quad (24)$$

5.2. Currents IP Controllers

Parameters for the *d*-*q* axis current controllers

$$\begin{cases} k_i = \frac{94\sigma L_s}{\gamma} \\ k_p = 24\gamma \end{cases} \quad (25)$$

Parameters for the *x*-*y* axis current controllers

$$\begin{cases} k_i = 94R_s \\ k_p = \frac{24}{L_{ls}} R_S \end{cases} \quad (26)$$

5.3. Flux IP Controller

The Formula (27) presents the parameters of the flux controller.

$$\begin{cases} k_i = \frac{94}{L_m} \\ k_p = \frac{24}{T_r} \end{cases} \quad (27)$$

6. Theory for SMC Based DFOC for FPIM

The robustness of SMC relies on its intrinsic ability to maintain stable control despite the presence of uncertainties, disturbances, and variations in the system dynamics. This robustness primarily stems from the key characteristics of the control technique [23,31,63,64]:

- ✔ Sliding surface: SMC utilizes a sliding surface to guide the trajectory of the system state in tracking a desired reference trajectory. The sliding surface acts as a "virtual wall" that the system is compelled to follow. This means that, regardless of the inherent uncertainties of the system or external disturbances, the control action is designed to keep the system state on this sliding surface.
- ✔ Discontinuous control action: SMC employs a discontinuous control law that switches the control action to keep the system on the sliding surface. This control action changes instantaneously, essentially ignoring small perturbations and focusing on maintaining the system on the sliding surface.
- ✔ Invariance principle: The essential foundation of SMC lies in the invariance principle, stating that once the system reaches the sliding surface, it will remain there indefinitely. This invariance ensures that the system maintains its robustness against uncertainties and disturbances, as it is designed to stay on the sliding surface regardless of external influences.
- ✔ Chattering: Although chattering is generally considered an undesirable feature of SMC, it contributes to the robustness of the control approach. Chattering helps mitigate uncertainties and disturbances by quickly adapting the control action to the changing dynamics of the system.

The concept of SMC consists of three phases: an initial reaching phase, where the state trajectory is directed towards the surface S = 0 and reaches it in a finite time. This is followed by a sliding phase, where the trajectory slides on the switching surface towards an equilibrium point. The fundamental principle of SMC is illustrated in Figure 7 [65,66].

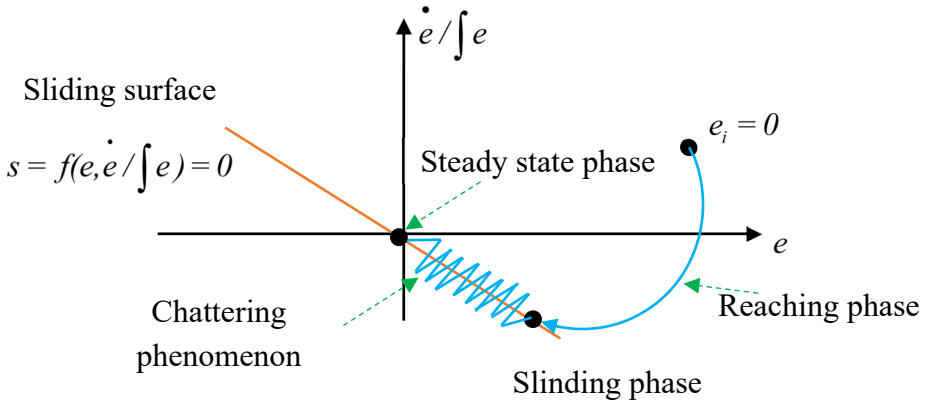

Figure 7. State trajectory with respect to sliding surface.

In this context, the SMC law consists of two terms [67]:

$$u = u_{eq} + u_{nl} \tag{28}$$

- ⇨ A continuous term "u_{eq}" describing the system dynamics on the sliding surface.
- ⇨ A discontinuous term "u_{nl}" describing the system dynamics during the reaching mode.

To synthesize an SMC law, the following steps should be followed [22,25,67]:

(i) Choosing of the sliding surfaces,
(ii) Establishing a control strategy to guide the system state trajectory towards a predefined surface within a finite time,
(iii) Verifying the stability conditions that can be defined by applying the Lyapunov function.

6.1. Synthesis of Speed CSMC

According to the SMC theory, the control law that describes the reference electromagnetic torque is defined as follows [14,22,23]:

$$T_e{}^* = T_{eeq} + T_{enl} \tag{29}$$

where T_{eeq} and T_{enl} respectively represent the equivalent part and the non-linear part of the reference torque $T_e{}^*$. The chosen sliding surface is defined by the speed error, as illustrated by (30):

$$\begin{cases} S_\Omega = \Omega - \Omega^* \\ \dot{S}_\Omega = \dot{\Omega} - \dot{\Omega}^* \end{cases} \tag{30}$$

The main objective is that the actual speed Ω should track its reference.

Inserting (3) into the speed sliding surface derivative equation provided by (30), we obtain:

$$\dot{S}_\Omega = \frac{1}{J}(T_e - T_L - f\Omega) - \dot{\Omega}^* \tag{31}$$

where J, f, T_L and T_e denote the inertia moment, the coefficient of friction, the load torque, and the electromagnetic torque, respectively.

The necessary condition for the state of the system to follow the trajectory defined by the sliding surface is $S_\Omega = \dot{S}_\Omega = 0$. This condition gives:

$$T_{eeq} = T_L + f\Omega + J\dot{\Omega}^* \tag{32}$$

A discontinuous control action, defined by the term T_{enl}, is established to guarantee finite time convergence towards the sliding surface, despite uncertainties and disturbances. The discontinuous control is defined by (33):

$$T_{enl} = K_\Omega sign(S_\Omega) \tag{33}$$

where K_Ω is a positive proportional gain of non-linear control relative to the speed controller, and $sign(.)$ is a sign function. Finally, the reference torque $T_e{}^*$ is defined by this equation:

$$T_e^* = T_L + f\Omega + J\dot{\Omega}^* - K_\Omega sign(S_\Omega) \tag{34}$$

To check system stability, we use the Lyapunov function V, which is defined by (35) [68]:

$$V = \frac{1}{2}S_\Omega^2 \tag{35}$$

If the time derivative of the Lyapunov function V is negative, it implies that $\dot{V}(x) < 0$ for all $x \neq 0$, in this scenario, we can confirm the conditions for the existence and achievability of the sliding mode. Then, we differentiate V with respect to time as follows [14]:

$$\dot{V} = S_\Omega \dot{S}_\Omega < 0 \tag{36}$$

To verify the reachability condition of speed SMC, we can follow the steps outlined below. By (35) with (32), we obtain the desired result in (37):

$$\dot{S}_\Omega = -\frac{K_\Omega}{J} sign(S_\Omega) \tag{37}$$

Referring to (36), it can be rewritten as:

$$S_\Omega \dot{S}_\Omega = S_\Omega(-\frac{K_\Omega}{J} sign(S_\Omega)) < 0 \tag{38}$$

With

$$S_\Omega(sign(S_\Omega)) = |S_\Omega| > 0 \tag{39}$$

Using (38) and (39), we can obtain the following condition:

$$-\frac{K_\Omega}{J}|S_\Omega| < 0 \rightarrow \frac{K_\Omega}{J} > 0 \tag{40}$$

To ensure the stability of the speed controller, it is necessary to adjust gain in a way that satisfies the inequality stated in (40).

6.2. Synthesis of Flux CSMC

Based on references [14,22,23], defining the SMC theory and the steps required for SMC design as follows in Section 6 of this document, the control law and stability condition of Flux CSMC are developed as shown below:

Flux CSMC generates the direct reference stator current i_{sd}^*. The equivalent part and non-linear part of the reference i_{sd}^* are denoted and represented as follows:

$$i_{sd}^* = i_{sdeq} + i_{sdnl} \tag{41}$$

To determine the control law i_{sd}^*, the sliding surface associated with the flux controller is given by the following expression:

$$S_{\psi_r} = \psi_r - \psi_r^* \tag{42}$$

Equation (42) can be differentiated with respect to time, resulting in the following time derivative:

$$\dot{S}_{\psi_r} = \dot{\psi}_r - \dot{\psi}_r^* \tag{43}$$

From (5) we obtain:

$$\dot{\psi}_r = \frac{L_m}{T_r} i_{sd} - \frac{1}{T_r}\psi_r \tag{44}$$

By substituting (44) into (43), we obtain:

$$\dot{s}_{\psi_r} = \frac{L_m}{T_r} i_{sd} - \frac{1}{T_r}\psi_r - \dot{\psi}_r^* \tag{45}$$

The condition necessary to fulfill the sliding mode is articulated as follows:

$$\dot{s}_{\psi_r} = s_{\psi_r} = 0 \tag{46}$$

From (46) and (45), the equivalent part of the reference current i_{sd}^* is represented as follows:

$$i_{sdeq} = \frac{1}{L_m}\psi_r + \frac{T_r}{L_m}\dot{\psi}_r^* \tag{47}$$

The non-linear part of the reference i_{sd}^* is as follows:

$$i_{sdnl} = K_{\psi_r} sign\left(S_{\psi_r}\right) \;\; with \;\; 0 < \alpha < 1 \tag{48}$$

The global control is as follows:

$$i_{sd}^* = \frac{1}{L_m}\psi_r + \frac{T_r}{L_m}\dot{\psi}_r^* + K_{\psi_r} sign(S_{\psi_r}); \quad L_m > 0 \tag{49}$$

To analyze the stability of the suggested approach, the Lyapunov function can be employed, as given by (35). Thus, by substituting (49) into (45), we can obtain:

$$\dot{S}_{\psi_r} = -\frac{L_m}{T_r} K_{\psi_r} sign(S_{\psi_r}) \tag{50}$$

Using (36), the Lyapunov condition is given by:

$$S_{\psi_r}\dot{S}_{\psi_r} = S_{\psi_r}(-\frac{L_m}{T_r}K_{\psi_r}sign(S_{\psi_r})) < 0 \tag{51}$$

Moreover,

$$S_{\psi_r}sign(S_{\psi_r}) = |S_{\psi_r}| \tag{52}$$

Using (52) and (51) we obtain:

$$S_{\psi_r}\dot{S}_{\psi_r} = -\frac{L_m}{T_r}K_{\psi_r}|S_{\psi_r}| < 0 \tag{53}$$

Knowing that $|S_{\psi_r}|$ is always positive, we obtain:

$$K_{\psi_r} > \frac{T_r}{L_m} \tag{54}$$

To guarantee the stability of the flux controller, it is essential to fine-tune gain K_{ψ_r} so that it can meet the conditions of (54).

6.3. Synthesis of Direct Stator Current CSMC

The direct stator current controller supplies voltage v_{sd}, which represents the first term of the control reference voltage v_{sd}^*, as given by (9). Based on references [55] and the beginning of Section 6 of this document, the global control law of the direct stator current controller is defined as follows:

$$v_d^* = v_{deq} + v_{dnl} \tag{55}$$

where v_{deq} is the equivalent part of the control law, and v_{dnl} is the non-linear part of the control law.

To compute the control law v_{deq}, the sliding surface associated with the direct stator current controller i_{sd} is given by:

$$S_{i_{sd}} = i_{sd} - i_{sd}^* \tag{56}$$

The time derivative of (56) is expressed as follows:

$$\dot{S}_{i_{sd}} = \dot{i}_{sd} - \dot{i}_{sd}^* \tag{57}$$

From (10), we obtain the expression for:

$$\dot{i}_{sd} = \frac{v_d}{\sigma L_s} - \gamma i_{sd} \tag{58}$$

By substituting (58) into (57), we obtain:

$$\dot{s}_{isd} = \frac{v_d}{\sigma L_s} - \gamma i_{sd} - \dot{i}_{sd}^* \tag{59}$$

The condition required to meet the sliding mode is presented as follows:

$$s_{i_{sd}} = \dot{s}_{i_{sd}} = 0 \tag{60}$$

According to (55)–(60), the control law of the equivalent part and the global control law are given by (61) and (62), respectively:

$$v_{deq} = \sigma L_s(\gamma i_{sd} + i_{sd}^*) \tag{61}$$

$$v_d^* = \sigma L_s(\gamma i_{sd} + i_{sd}^*) - K_d sign(S_{i_{sd}}) \tag{62}$$

K_d: proportional gain of nonlinear control with respect to the direct stator current controller. To assess system stability, we employ the Lyapunov function, which is defined as follows [67]:

$$V_{i_{sd}} = \frac{1}{2} S_{i_{sd}}^2 \tag{63}$$

Moreover, the stability condition is given by the following equation:

$$\dot{V}_{i_{sd}} = \dot{S}_{i_{sd}} \dot{S}_{i_{sd}} \tag{64}$$

By substituting (62) into (59), we obtain:

$$\dot{S}_{i_{sd}} = -\frac{K_d}{\sigma L_s} sign(S_{i_{sd}}) \tag{65}$$

Using (64), the Lyapunov condition is calculated as follows:

$$S_{i_{sd}} \dot{S}_{i_{sd}} = -S_{i_{sd}} \frac{K_d}{\sigma L_s} sign(S_{i_{sd}}) \prec 0 \tag{66}$$

With

$$S_{i_{sd}} sign(S_{i_{sd}}) = |S_{i_{sd}}| \tag{67}$$

$|S_{i_{sd}}|$ is always positive, i.e., the stability condition is only satisfied when:

$$\frac{K_d}{\sigma L_s} > 0 \tag{68}$$

6.4. Synthesis of Quadratic Stator Current CSMC

The quadratic stator current controller supplies the first term v_q^* of the quadratic reference stator voltage v_{sq}^* given by (9).

The global law for the quadratic stator current controller is defined as follows, based on references [67] and Section 6 of this document:

$$v_q^* = v_{qeq} + v_{qnl} \tag{69}$$

with:

v_{qeq}: the equivalent part of the control law,
v_{qnl}: the non-linear part of the control law.

In order to determine the control law v_{qeq}, the sliding surface associated with the quadratic stator current controller is as follows:

$$S_{i_{sq}} = i_{sq} - i_{sq}^* \tag{70}$$

The time derivative of Equation (70) is expressed as follows:

$$\dot{S}_{i_{sd}} = \dot{i}_{sd} - \dot{i}_{sd}^* \tag{71}$$

From (10), we derive the following expression:

$$\dot{i}_{sq} = \frac{v_q}{\sigma L_s} - \gamma i_{sq} \tag{72}$$

Inserting (72) into (71), we obtain:

$$\dot{s}_{isq} = \frac{v_d}{\sigma L_s} - \gamma i_{sq} - i_{sq}^* \tag{73}$$

By applying the necessary condition to satisfy the sliding mode defined by (60) and (69)–(73), the control law of the equivalent part and the global control law are given by (74) and (75), respectively:

$$v_{qeq} = \sigma L_s \left(\gamma i_{sq} + i_{sq}^* \right) \tag{74}$$

$$v_q^* = \sigma L_s \left(\gamma i_{sq} + i_{sq}^* \right) - K_q sign(S_{i_{sq}}) \tag{75}$$

K_q: Positive proportional gain.

To evaluate the stability of the system, we utilize the Lyapunov function, defined as follows:

$$V = \frac{1}{2} S_{iq}^2 \tag{76}$$

In addition, the stability condition is expressed by the following equation:

$$\dot{V} = S_{i_{sq}} \dot{S}_{i_{sq}} \prec 0 \tag{77}$$

Upon substituting (75) into (73), we obtain:

$$\dot{S}_{i_{sq}} = -\frac{K_d}{\sigma L_s} sign(S_{i_{sq}}) \tag{78}$$

Using (77), the Lyapunov condition is calculated as follows:

$$S_{i_{sq}} \dot{S}_{i_{sq}} = -S_{i_{sq}} \frac{K_d}{\sigma L_s} sign(S_{i_{sq}}) \prec 0 \tag{79}$$

With:

$$S_{i_{sq}} sign\left(S_{i_{sq}} \right) = \left| S_{i_{sq}} \right| \tag{80}$$

Term $|S_{isd}|$ is always positive, i.e., the stability condition is only satisfied when:

$$\frac{K_q}{\sigma L_s} > 0 \tag{81}$$

6.5. Synthesis of i_{sx} and i_{sy} Direct Stator Current CSMC

The two current controllers i_{sx} and i_{sy} supply the reference voltages v_{sx}^* and v_{sy}^* respectively. Referring to (5) and Section 6 of this document, the global control law of v_{sx}^* and v_{sy}^* are expressed by:

$$\begin{cases} v_{sx}^* = v_{sxeq} + v_{sxnl} \\ v_{sy}^* = v_{syeq} + v_{synl} \end{cases} \tag{82}$$

To calculate the two control laws v_{sx}^* and v_{sy}^*, we define the two slip surfaces S_{sx} and S_{sy}, respectively linked to the i_{sx} and i_{sy} current controllers:

$$\begin{cases} S_{sx} = i_{sx} - i_{sx}^* \\ S_{sy} = i_{sy} - i_{sy}^* \end{cases} \tag{83}$$

The time derivative of (83) gives us:

$$\begin{array}{l} \dot{S}_{sx} = \dot{i}_{sx} - \dot{i}_{sx}^* \\ \dot{S}_{sy} = \dot{i}_{sy} - \dot{i}_{sy}^* \end{array} \tag{84}$$

From (5), the i_{sx} and i_{sy} currents are expressed as follows:

$$\begin{cases} \dot{i}_{sx} = -\frac{R_s}{L_{ls}} i_{sx} + \frac{1}{L_{ls}} v_{sx} \\ \dot{i}_{sy} = -\frac{R_s}{L_{ls}} i_{sy} + \frac{1}{L_{ls}} v_{sy} \end{cases} \tag{85}$$

By substituting (85) into (84), we obtain:

$$\begin{cases} \dot{S}_{sx} = -\frac{R_s}{L_{ls}} i_{sx} + \frac{1}{L_{ls}} v_{sx} - \dot{i}^*_{sx} \\ \dot{S}_{sy} = -\frac{R_s}{L_{ls}} i_{sy} + \frac{1}{L_{ls}} v_{sy} - \dot{i}^*_{sy} \end{cases} \tag{86}$$

The application of the sliding surface ($\dot{S} = S = 0$) results in:

$$\begin{cases} v_{eqsx} = R_S i_{sx} + L_{ls} i^*_{sx} \\ v_{eqsy} = R_S i_{sy} + L_{ls} i^*_{sy} \end{cases} \tag{87}$$

And

$$\begin{cases} v^*_{sx} = R_S i_{sx} + L_{ls} \dot{i}^*_{sx} - K_{sx} sign(S_{sx}) \\ v^*_{sy} = R_S i_{sy} + L_{ls} \dot{i}^*_{sy} - K_{sy} sign(S_{sy}) \end{cases} \tag{88}$$

To assess the system stability, we use the Lyapunov condition, which is defined as follows:

$$\begin{cases} S_{i_{sx}} \dot{S}_{i_{sx}} < 0 \\ S_{i_{sy}} \dot{S}_{i_{sy}} < 0 \end{cases} \tag{89}$$

Inserting (88) into (86) yields:

$$\begin{cases} \dot{S}_{sx} = -\frac{K_{sx}}{L_{ls}} sign(S_{sx}) \\ \dot{S}_{sy} = -\frac{K_{sy}}{L_{ls}} sign(S_{sy}) \end{cases} \tag{90}$$

And

$$\begin{cases} S_{sx} \dot{S}_{sx} = -\frac{K_{sx}}{L_{ls}} S_{sx} sign(S_{sx}) \\ S_{sy} \dot{S}_{sy} = -\frac{K_{sy}}{L_{ls}} S_{sy} sign(S_{sy}) \end{cases} \tag{91}$$

With:

$$\begin{cases} S_{sx} sign(S_{sx}) = |S_{sx}| > 0 \\ S_{sy} sign(S_{sy}) = |S_{sy}| > 0 \end{cases} \tag{92}$$

The stability condition defined by (77) is satisfied only when:

$$\begin{cases} \frac{K_{sx}}{L_{ls}} > 0 \\ \frac{K_{sy}}{L_{ls}} > 0 \end{cases} \tag{93}$$

Remark: The "sign" function presented in Equations (33), (34), (49) and (75) induces the chattering phenomenon [31–33]. In fact, this phenomenon can be mitigated by replacing this function with "saturation" or "sigmoid" functions, but precision is lost [19]. To achieve smooth control signals with reduced chattering, a second sliding mode control technique based on the super-twisting algorithm will be developed and applied to the FPIM.

6.6. SOSMC Theory

In this section, we propose a new SOSMC control law that reduces disturbances caused by changes or fluctuations in the parameters of FPIM. In an FPIM, the parameters can vary due to external factors, such as temperature, wear, humidity, etc. These variations can affect the dynamics of the FPIM, resulting in undesirable disturbances in the operation of the FPIM.

In the context of SMC, the control law is designed to mitigate the effects of disturbances caused by these parametric variations. The objective is to make the system robust against these variations so that it can maintain its desired behavior despite changes in its parameters.

By using an appropriate combination of the equivalent control law $u_{eq}(t)$ and the STA law $u_{ST}(t)$, we can reduce the impact of parametric variations and the phenomenon of

chattering that may occur when control is unstable or exhibits undesirable oscillations. Integrating these two control laws provides a more robust approach to regulating the system and mitigating disturbances caused by parametric variations [14,23].

$$u(t) = u_{eq}(t) + u_{ST}(t) \tag{94}$$

The STA u_{ST} is a second-order sliding mode. This controller slides on the space $s = \dot{s} = 0$ using only the measurement of s without needing information on the time derivative of the sliding surface s. The second-order super-twist algorithm defines the control law as the sum of two terms. The first is defined by the integral of a discontinuous function of the slip surface variable, while the second is a continuous function of the slip surface variable to reduce the chattering effect [14,31,33]. The STA is defined as follows [23,32,50].

$$\begin{cases} u_{ST} = -\lambda |s|^{\alpha} sign(s) + u_1 \\ \dot{u}_1 = -\beta sign(s) \end{cases} \tag{95}$$

where (s) is the sliding surface and the value of the parameter α comprises between 0 and 0.5. The parameters λ and β are the gains of the STA. These gains are positive constants [69]. The convergence of the control law that represents the STA is obtained by adjusting the values of λ and β, which have effects on the steady-state response and accuracy of the system, respectively. The sufficient conditions that ensure finite-time convergence are set by Levant in [48] as follows.

$$\begin{cases} \beta > \frac{\Phi}{\Gamma_M} \\ \lambda^2 \geq \frac{4\Phi\Gamma_M(\beta+\Phi)}{\Gamma_m^3(\beta-\Phi)} \end{cases} \tag{96}$$

where β, λ, Φ, and Γ_M are positive constants, Φ is the positive bound of the uncertain function Φ, and Γ_M and Γ_m are the upper and lower positive bounds of the uncertain function γ to the second derivative of the sliding surface given as follows [69].

$$\ddot{S} = \phi(x,t) + \gamma(x,t)\dot{u} \tag{97}$$

To guarantee the convergence of the sliding surface to zero in the presence of disturbances and uncertainties, functions $\phi(x,t)$ and $\gamma(x,t)$ must satisfy the following conditions: $\Phi \geq |\phi|$ and $\Gamma_M \geq \gamma \geq \Gamma_m > 0$ [68,69].

6.7. Synthesis of Speed SOSMC-STA

Applying uncertainties, $\Delta\left(\frac{1}{J}\right)$, $\Delta\left(\frac{T_L}{J}\right)$, and $\Delta\left(\frac{f}{J}\right)$ in the quantities $\frac{1}{J}$, $\frac{T_L}{J}$ and $\frac{f}{J}$, respectively, in Equation (3), we obtain the following equation [23]:

$$\dot{\Omega} = \frac{T_e}{J} - \frac{T_L}{J} - \frac{f}{J}\cdot\Omega + \Delta\left(\frac{1}{J}\right)T_e + \Delta\left(\frac{T_L}{J}\right) + \Delta\left(\frac{f}{J}\right)\Omega\dot{\Omega} = \frac{T_e}{J} - \frac{T_L}{J} - \frac{f}{J}\cdot\Omega + \Delta\dot{\Omega} \tag{98}$$

where, $\Delta\dot{\Omega} = \Delta\left(\frac{1}{J}\right)T_e + \Delta\left(\frac{T_L}{J}\right) + \Delta\left(\frac{f}{J}\right)\Omega$, represents the perturbation term. The sliding surface, s_Ω, is defined as the error, e(t), between the reference speed Ω^* and the actual speed Ω, as follows:

$$\begin{cases} S_\Omega = \Omega - \Omega^* \\ \\ \dot{S}_\Omega = \dot{\Omega} - \dot{\Omega}^* \end{cases} \tag{99}$$

The required condition to achieve sliding mode is presented as follows:

$$S_\Omega = \dot{S}_\Omega = 0 \tag{100}$$

From (94), (95), (98), and (100) the reference torque generated by the speed SOSMC-STA speed is given by the following equation:

$$T_{e-ref} = T_L + f\Omega + J\dot{\Omega}^* - J\Delta\dot{\Omega} \tag{101}$$

Referring to [23] and (94), the disturbance term is defined as follows:

$$-J\Delta\dot{\Omega} = u_{ST}(t) \tag{102}$$

By inserting (102) into (101), we obtain:

$$T_{e-ref} = T_L + f\Omega + J\dot{\Omega}^* - \lambda_\Omega |s|^{\frac{1}{2}} sign(s_\Omega) - \beta_\Omega \int sign(s_\Omega) dt \tag{103}$$

Substituting (103) into (99) gives us:

$$\begin{cases} \dot{s}_\Omega = -\frac{\lambda_\Omega}{J}|s|^{\frac{1}{2}} sign(s_\Omega) + u + \Delta\dot{\Omega} \\ \dot{u} = -\frac{\beta_\Omega}{J} sign(s_\Omega) \end{cases} \tag{104}$$

We assumed that: $s_\Omega = z_1, u = z_2, \Delta(\dot{\Omega}) = \varepsilon, \frac{\lambda_\Omega}{J} = k_1 et \frac{\beta_\Omega}{J} = k_2$.
The Equation (104) can be rewritten as follows:

$$\begin{cases} \dot{z}_1 = -k_1 |z_1|^{\frac{1}{2}} sign(z_1) + z_2 + \varepsilon \\ \dot{z_2} = -k_2 sign(z_1) \end{cases} \tag{105}$$

Following [70–72], the stability analyses of the super-twisting speed controller represented by (105) are given as follows:
The candidate Lyapunov function for the perturbed system (105) is as follows [71]:

$$V(z) = 2k_3|z_1| + \frac{1}{2}z_2^2 + \frac{1}{2}\left(k_1|z_1|^{\frac{1}{2}} sign(z_1) - z_2\right)^2 \tag{106}$$

According to [71], the disturbance term of the system (105) is given by (107).

$$|\epsilon| \leq \delta |Z_1|^{\frac{1}{2}},\ \delta \geq 0 \tag{107}$$

The proposed Lyapunov function given by (106) can be expressed in quadratic form as follows:

$$V(z) = X^T P X \tag{108}$$

where $X^T = [X_1, X_2]^T = [|z_1|^{\frac{1}{2}} sign(z_1), z_2]^T$, $P = \frac{1}{2}\begin{bmatrix} 4k_2 + k_1 & -k_1 \\ -k_1 & 2 \end{bmatrix}$.
Since P is a positive definite symmetric matrix, we can establish the following inequality.

$$\lambda_{min}\{P\}\|Z\|_2^2 \leq V \leq \lambda_{max}\{P\}\|Z\|_2^2 \tag{109}$$

where $\lambda_{min}\{P\}$ and $\lambda_{max}\{P\}$ respectively represent the smallest and largest eigenvalues of the matrix P. and $\|.\|_2$ corresponds to the Euclidean norm of a vector.
The time derivative of X along the trajectories of the system (105) is computed in the following manner:

$$\dot{X} = \begin{pmatrix} \dot{X}_1 \\ \dot{X}_2 \end{pmatrix} = \frac{1}{|X_1|}\left(\begin{bmatrix} -\frac{1}{2}k_1 & \frac{1}{2} \\ -k_3 & 0 \end{bmatrix}\begin{pmatrix} X_1 \\ X_2 \end{pmatrix} + \begin{pmatrix} 1 \\ 0 \end{pmatrix}|X_1|\epsilon\right) \tag{110}$$

where: $\begin{bmatrix} -\frac{1}{2}k_1 & \frac{1}{2} \\ -k_3 & 0 \end{bmatrix} = A, \binom{1}{0} = B$ and $|X_1|\epsilon = \varphi$.

$$\dot{X} = \frac{1}{|X_1|}(AX + B\varphi) \tag{111}$$

The time derivative of V along the trajectories of the X dynamics is computed as follows:

$$\dot{V} = X^T P\dot{X} + \dot{X^T} PX\dot{V} = \frac{1}{|X_1|}\begin{pmatrix} X \\ \varphi \end{pmatrix}^T \begin{bmatrix} A^T P + PA & PB \\ B^T P & 0 \end{bmatrix} \begin{pmatrix} X \\ \varphi \end{pmatrix} \tag{112}$$

According to (107), the following inequality is observed.

$$0 \leq \delta^2 |X_1|^2 - \varphi^2 \tag{113}$$

By adding (113) to the second term of (112), we obtain the inequality given by (114).

$$\begin{gathered} \dot{V} \leq \tfrac{1}{|X_1|}\left(\binom{X}{\varphi}^T \begin{bmatrix} A^T P + PA & PB \\ B^T P & 0 \end{bmatrix} \binom{X}{\varphi} + \delta |X_1|^2 - \varphi^2 \right) \\ \dot{V} \leq \tfrac{1}{|X_1|}\left(\binom{X}{\varphi}^T \begin{bmatrix} A^T P + PA + \delta C & PB \\ B^T P & -1 \end{bmatrix} \binom{X}{\varphi} \right) \\ \dot{V} \leq -\tfrac{1}{|X_1|} X^T Q X \end{gathered} \tag{114}$$

where

$$C = \begin{bmatrix} 1 & 0 \\ 0 & 0 \end{bmatrix}$$

And

$$\widetilde{Q} = \frac{k_1}{2}\begin{pmatrix} 2k_2 + k_1^2 - \left(4\frac{k_2}{k_1} + k_1\right)\delta & -(k_1 + 2\delta) \\ -(k_1 + 2\delta) & 1 \end{pmatrix}$$

The time derivative of V is considered negative if $\widetilde{Q} > 0$. It is clear that this holds true when the gains satisfy the inequality defined by (115) below [71,72].

$$k_1 > 2\delta k_2 > k_1 \frac{5\delta k_1 + 4\delta^2}{2(k_1 - 2\delta)} \tag{115}$$

Q is a positive definite symmetric matrix. Consequently, this inequality is established.

$$\dot{V} \leq -\frac{1}{|X_1|} X^T Q X \leq -\frac{1}{X_1} \lambda_{min}\{Q\} \|X\|_2^2 \leq -\check{\gamma}\sqrt{V} \tag{116}$$

where $\lambda_{min}\{Q\}$ denotes the smallest eigenvalue of Q, and $\check{\gamma}$ is a positive constant given by the following expression [71].

$$\check{\gamma} = \frac{\lambda_{min}\{Q\}\sqrt{\lambda_{min}\{P\}}}{\lambda_{max}\{P\}} \check{T} = \frac{2V^{\frac{1}{2}}(z_0)}{\check{\gamma}} \tag{117}$$

According to [71–73] and following (115) and (117), z_1 and z_2 converge to the origin in a finite time.

6.8. Synthesis of Flux SOSMC-STA

According to (47), (94), and (95), the reference direct stator current generated by the Flux SOSMC-STA is:

$$i_{sd-ref} = \frac{1}{L_m}\psi_r + \frac{T_r}{L_m}\dot{\psi}_r^* - \lambda_{\psi_r}|s_{\psi_r}|^{\frac{1}{2}}sign(s_{\psi_r}) - \beta_{\psi_r}\int sign(s_{\psi_r})dt \quad (118)$$

The direct stator current control law given by (118) must satisfy the Lyapunov stability condition presented by (51) to ensure flux control stability. The substitution of (118) into (45) yields:

$$\dot{s}_{\psi_r} = -\frac{L_m}{T_r}\lambda_{\psi_r}|s_{\psi_r}|^{\frac{1}{2}}sign(s_{\psi_r}) - \frac{L_m}{T_r}\beta_{\psi_r}\int sign(s_{\psi_r})dt \quad (119)$$

Next, the Lyapunov stability condition is as follows:

$$s_{\psi_r}\dot{s}_{\psi_r} = -\frac{L_m}{T_r}\lambda_{\psi_r}s_{\psi_r}|s_{\psi_r}|^{\frac{1}{2}}sign(s_{\psi_r}) - \frac{L_m}{T_r}\beta_{\psi_r}s_{\psi_r}\int sign(s_{\psi_r})dt \quad (120)$$

Therefore, according to (51), the flux control stability condition is satisfied only when $\frac{L_m}{T_r}\lambda_{\psi_r} > 0$ and $\frac{L_m}{T_r}\beta_{\psi_r} > 0$.

6.9. Synthesis of Direct Stator Current SOSMC-STA

Respecting (61), (94), and (95), the reference direct voltage generated by the direct stator current SOSMC-STA is as follows:

$$v_{d-ref} = \sigma L_s(\gamma i_{sd} + i_{sd}^*) - \lambda_{v_d}|s_{isd}|^{\frac{1}{2}}sign(s_{isd}) - \beta_{v_d}\int sign(s_{isd})dt \quad (121)$$

The direct stator voltage control law given by (121) must satisfy the Lyapunov stability condition presented by (51) to ensure direct stator current control stability. By introducing (121) into (59), we obtain:

$$\dot{s}_{isd} = -\frac{\lambda_{v_d}}{\sigma L_s}|s_{isd}|^{\frac{1}{2}}sign(s_{isd}) - \frac{\beta_{v_d}}{\sigma L_s}\int sign(s_{isd})dt \quad (122)$$

According to the Lyapunov stability condition, the direct stator current control stability is guaranteed only when $\frac{\lambda_{v_d}}{\sigma L_s} > 0$ and $\frac{\beta_{v_d}}{\sigma L_s} > 0$.

6.10. Synthesis of Quadratic Stator Current SOSMC-STA

Applying uncertainties, $\Delta\left(\frac{1}{\sigma L_s}\right)$, $\Delta(\gamma)$ in terms $\frac{1}{\sigma L_s}$, and γ, respectively, in Equation (72), we obtain [23]:

$$\dot{i}_{sq} = \frac{v_q}{\sigma L_s} - \gamma i_{sq} + \Delta i_{sq} \quad (123)$$

where $\Delta i_{sq} = \Delta\left(\frac{1}{\sigma L_s}\right)v_q - \Delta(\gamma)i_{sq}$.

Based on (94), (95), and (123), the reference quadratic voltage generated by the quadratic stator current SOSMC-STA is as follows [23]:

$$v_{q-ref} = \sigma L_s\left(\gamma i_{sq} + i_{sq}^*\right) - \lambda_{v_q}|s|^{\frac{1}{2}}sign(s) - \beta_{v_q}\int sign(s)dt + \Delta v \quad (124)$$

where $\Delta v = \sigma L_S \cdot \Delta i_{sq}$.

By substituting (124) into (73), we obtain:

$$\dot{s}_{isq} = -\frac{\lambda_{v_q}}{\sigma L_s}|s_{isq}|^{\frac{1}{2}}sign(s_{isq}) - \frac{\beta_{v_q}}{\sigma L_s}\int sign(s_{isq})dt + \Delta i_{sq} \quad (125)$$

The Equation (125) can be rewritten as follows:

$$\begin{cases} \dot{s}_{isq} = -\frac{\lambda_{vq}}{\sigma L_s}|s_{isq}|^{\frac{1}{2}} sign(s_{isq}) + u + \Delta i_{sq} \\ \dot{u} = -\frac{\beta_{vq}}{\sigma L_s} sign(s_{isq}) \end{cases} \tag{126}$$

We pose: $s_{isq} = z_{1i}, u = z_{2i}, \Delta v = \varepsilon_i, \frac{\lambda_{vq}}{\sigma L_s} = k_{1i} et \frac{\beta_{vq}}{\sigma L_s} = k_{2i}$.
We obtain the following system:

$$\begin{cases} \dot{z}_{1i} = -k_{1i}|z_1|^{\frac{1}{2}} sign(z_{1i}) + z_{2i} + \varepsilon_i \\ \dot{z_{2i}} = -k_{2i} sign(z_{1i}) \end{cases} \tag{127}$$

Respecting the steps of the stability analyses of the super-twisting speed controller represented by (105), the constants k_{1i} and k_{2i} that ensure the global asymptotic stability of the system (127) are given by (128).

$$k_{1i} > 2\delta i k_{2i} > k_1 \frac{5\delta i k_{1i} + 4\delta i^2}{2(k_{1i} - 2\delta i)} \tag{128}$$

where $|\epsilon_i| \leq \delta i |Z_{1i}|^{\frac{1}{2}}, \delta \geq 0$

According to (128) and (117), the variables z_{1i} and z_{2i} converge to the origin in finite time [71,72].

7. LMC for Efficiency Optimization of FPIM

The losses in asynchronous motors can be categorized into several types, including copper losses, iron losses, mechanical losses, and total losses. Copper losses are associated with ohmic losses in the stator and rotor windings. Iron losses are related to losses in the motor's ferromagnetic core. Mechanical losses are due to friction and ventilation losses. Total losses represent the sum of all these losses. Using the steady-state equivalent circuit of the FPIM with respect to the synchronous reference frame [6,49,51], the copper losses of the FPIM are given by the following expressions:

$$\begin{cases} p_s = R_s\left(i_{sd}^2 + i_{sq}^2\right) \\ p_r = R_r\left(i_{rd}^2 + i_{rq}^2\right) \end{cases} \tag{129}$$

The losses in the stator core are composed of hysteresis losses and eddy current losses.

$$p_{fs} = p_{hs} + p_{es} = k_h f_s \psi_s^2 + k_e f_s^2 \psi_s^2 \tag{130}$$

The losses in the rotor core p_{fr} are very low compared to the losses in the stator and are generally neglected.

with:

p_s, p_r: stator and rotor copper losses,
i_{sd}, i_{sq}: direct and quadrature components of stator current,
p_{fs}, p_{fr}: stator and rotor core losses,
p_{hs}, p_{es}: hysteresis and eddy current losses in stator,
k_h, k_e: are the hysteresis and eddy current coefficients related to magnetic circuit properties,
f_s: stator frequency.

The LMC strategy focuses on reducing the copper losses in the stator and rotor windings of the FPIM in the steady state by optimizing the rotor flux to achieve maximum efficiency. In this case, we will simplify the optimization process by neglecting the iron

losses. Consequently, the total copper losses in the FPIM are the sum of the stator and rotor copper losses [6,49].

$$p_{c-loss} = p_s + p_r = R_s\left(i_{sd}^2 + i_{sq}^2\right) + R_r\left(i_{rd}^2 + i_{rq}^2\right) \tag{131}$$

According to the FPIM-DFOC model given by (5) and (6), the steady-state flux ψ_r and the electromagnetic torque T_e are expressed as follows, respectively:

$$\dot{\psi}_r = 0 = -\frac{1}{T_r}\psi_r + \frac{L_m}{T_r}i_{sd} \rightarrow \psi_r = L_m i_{sd} \tag{132}$$

$$T_e = P.\frac{L_m}{L_r}.\left(\psi_r.i_{sq}\right) \tag{133}$$

From (132) and (133), we find:

$$\begin{cases} i_{sd} = \frac{\psi_r}{L_m} \\ i_{sq} = \frac{L_r T_e}{pL_m\psi_r} \end{cases} \tag{134}$$

Referring to [6,60], and respecting the DFOC control strategy, flows ψ_{rd} and ψ_{rq} are expressed respectively by the following equations:

$$\begin{cases} \psi_{rd} = \psi_r = L_r i_{rd} + L_m i_{sd} \\ \psi_{rq} = 0 = L_r i_{rq} + L_m i_{sq} \end{cases} \tag{135}$$

By introducing (132) and (134) into (135), we obtain:

$$\begin{cases} i_{rd} = 0 \\ i_{rq} = -\frac{T_e}{p\psi_r} \end{cases} \tag{136}$$

By substituting (134) and (136) into (131), we obtain:

$$p_{c-loss} = \frac{R_s}{(L_m)^2}\psi_r^2 + \left[\frac{R_r}{p^2} + R_s\left(\frac{L_r}{pL_m}\right)^2\right]\frac{T_e^2}{\psi_r^2} \tag{137}$$

In a steady-state condition, the optimal flux can be ascertained by equating the derivative of the total copper loss expression with respect to the rotor flux to zero.

$$\frac{\partial P_{c-loss}}{\partial \psi_r} = 0 \tag{138}$$

The solution to (138) gives:

$$\psi_{r-opt}^* = \lambda_{opt}\sqrt{T_e^*} \tag{139}$$

with: $\lambda_{opt} = \left(\frac{\lambda_2}{\lambda 1}\right)^{\frac{1}{4}}$ and $\lambda_1 = \frac{R_s}{L_m^2}$; $\lambda_2 = \frac{R_r}{p^2} + R_s\left(\frac{L_r}{pL_m}\right)^2$.

The diagram of the DFOC-SOSMC-STA based on LMC is given in Figure 8.

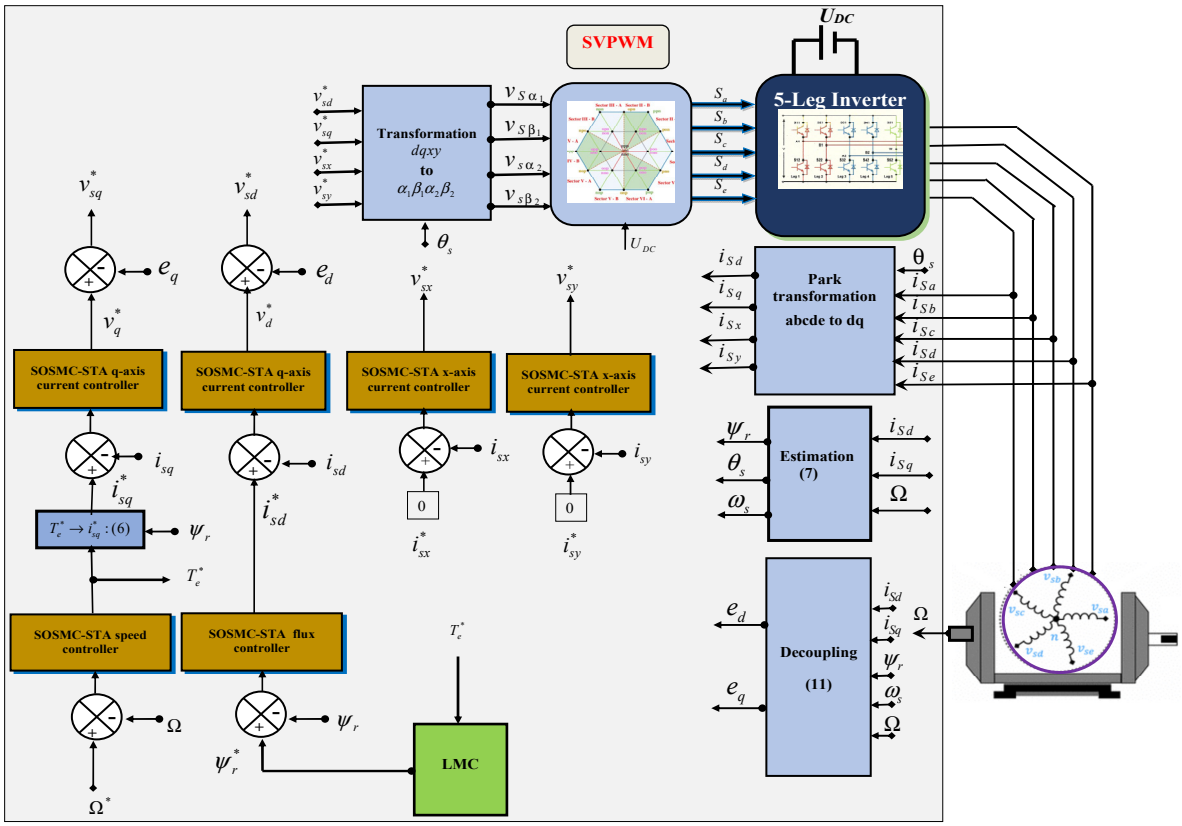

Figure 8. Structure of DFOC strategy for FPIM based on SOSMC-STAs and LMC.

8. Simulation Results and Discussion

The developed control algorithms are validated through numerical simulation using Matlab/Simulink R2018a software. The solver used in the Simulink model is ode8 (DORMAND-Prince), with a sampling time of 50×10^{-6}. The parameters and characteristics of the FPIM are presented in Tables A1 and A2 in Appendix A. In this section, we present and evaluate the simulation results of PICs, IPCs, CSMCs, and our proposed SOSMC-STAs-based DFOC approach for an FPIM. In the first case, the main objective is to attain better performance of the suggested SOSMC-STAs in terms of robustness, accuracy, fast response, etc. Indeed, these advantages include reducing oscillations/chattering in the electromagnetic torque and speed, precise tracking of reference speed and torque profiles, as well as their resistance to changes in load torque and rotor resistance.

In the second case, a loss minimization mechanism based on LMC is proposed and integrated into the suggested DFOC-SOSMC-STAs, with the goal of improving efficiency. Moreover, our DFOC-SOSMC-STAs strategy with the LMC mechanism is introduced in order to calculate the optimal rotor flux amplitude for each applied load torque. Thus, for evaluating the LMC performance, simulation studies are conducted with and without LMC to demonstrate the reduction in losses and the enhancement of FPIM efficiency when the LMC mechanism is employed.

Furthermore, additional criteria are employed for performance assessment: the Integral of Absolute Error (IAE), the Integral of Squared Error (ISE), and the Integral of Time multiplied by Absolute Error (ITAE). The speed errors are defined as follows:

$$e = \Omega - \Omega^* \tag{140}$$

Ω^* Represents the reference speeds for both machines, and Ω represents the actual speeds of the FPIM, respectively. IAE, ISE, and ITAE are defined as follows [74]:

$$\begin{cases} IAE = \int_0^t |e(t)|dt \\ ISE = \int_0^t e(t)^2 dt \\ ITAE = \int_0^t t|e(t)|dt \end{cases} \quad (141)$$

To demonstrate the effectiveness of both control strategies, a series of tests is carried out under various operating scenarios. The comparative study is consequently conducted across four distinct modes, as outlined below:

8.1. First Case: Performances Analysis of Suggested SOSMC-STAs in Steady State Operation

The objective of this study is to test, analyze, and compare the performance of PICs, IPCs, CSMCs, and our proposed SOSMC-STAs in terms of speed overshooting and dynamic response, accuracy in tracking, torque ripples, speed oscillations, stator current distortions, and robustness against sudden load torque variations. The test is conducted as follows:

The reference speed is set to 150 rad/s from 0.5 s to 8 s, and then to −150 rad/s from 8 s to 12 s. The load torque is fixed at 7.2 Nm applied at t = 5 s and kept constant until the end of the simulation. The parameters of the proposed controllers are provided in Appendix A (Table A2). The simulation results are presented in Figures 9–12.

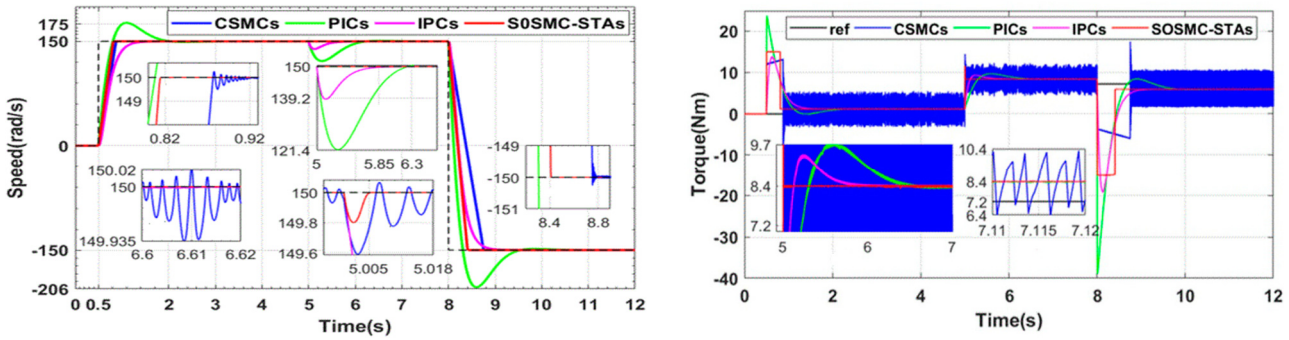

(**a**) (**b**)

Figure 9. DFOC based on PICs, IPCs, CSMCs, and the proposed SOSMC-STAs for (**a**) rotor speed and (**b**) electromagnetic torque response.

According to Figure 9a, it is clearly shown that the PICs exhibit unacceptable speed overshooting both during the setpoint application and during the direction reversal. However, this is not the case for the three other controllers. In fact, when the FPIM is controlled by the DFOC based on the IPCs, the CSMCs, and our proposed SOSMC-STAs, the actual speed converges to its reference without overshooting. Moreover, the static error of speed can be considered as neglected, thanks to the presence of the sign-type discontinuous control term in CSMCs and our SOSMC-STAs, as well as the integration of PICs and IPs. In addition, CSMCs and our SOSMC-STAs demonstrate robustness against load variations, while PICs and IPs are sensitive. Furthermore, referring to Figure 9a, it can be seen that the suggested SOSMC-STAs provide better performance in terms of fast convergence and robustness under sudden load torque applications and neglected oscillations around the reference speed. More details and comparisons are presented in Table 1.

Figure 9b illustrates the electromagnetic torque response provided by the FPIM when it is controlled through the aforementioned controllers. It can be seen that the proposed SOSMC-STAs converge rapidly to the load torque reference profile and exhibit significantly reduced chattering compared to the other controllers. In contrast, PICs and IPCs are characterized by relatively slow convergence, while the SMCs are fast, but exhibit chattering exceeding 40% of the nominal value. Therefore, the proposed SOSMC-STAs remain the best in terms of convergence speed and reduction of chattering phenomena compared to

the other tested controllers. For further clarification, a comparative study is provided in Table 1.

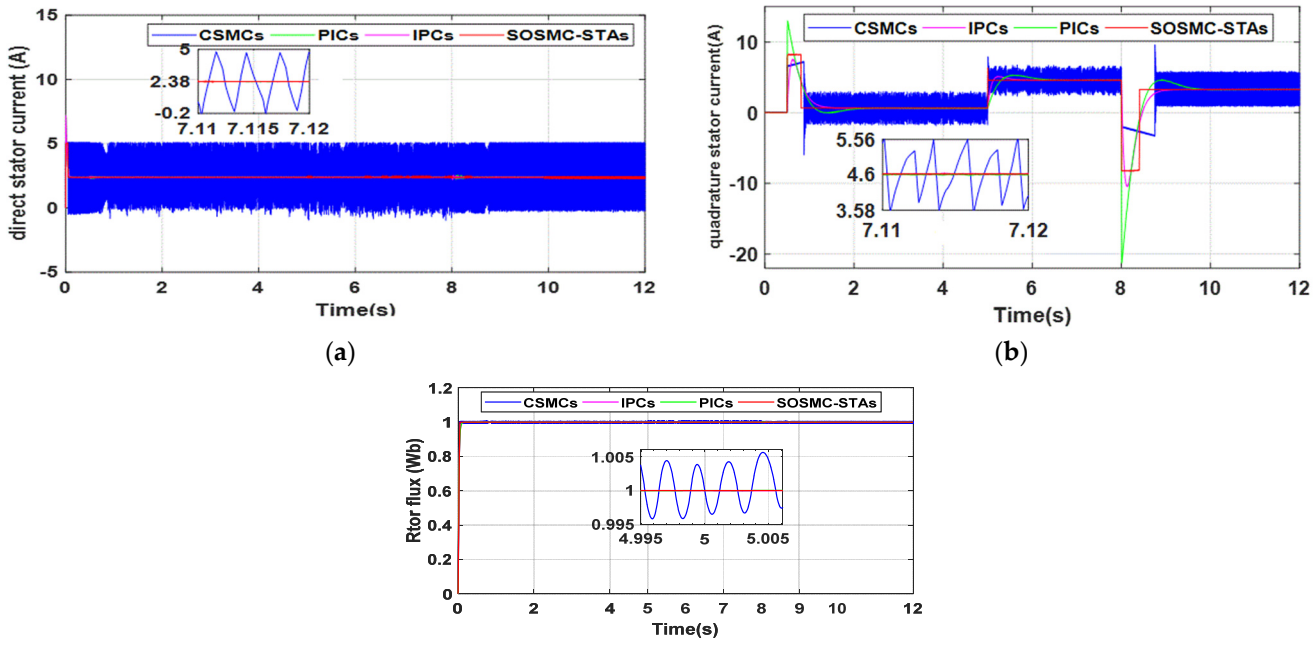

(**a**) (**b**)

(**c**)

Figure 10. DFOC based on PICs, IPCs, CSMCs, and the proposed SOSMC-STAs for (**a**) direct stator current response, (**b**) quadratic stator current response, and (**c**) rotor flux module.

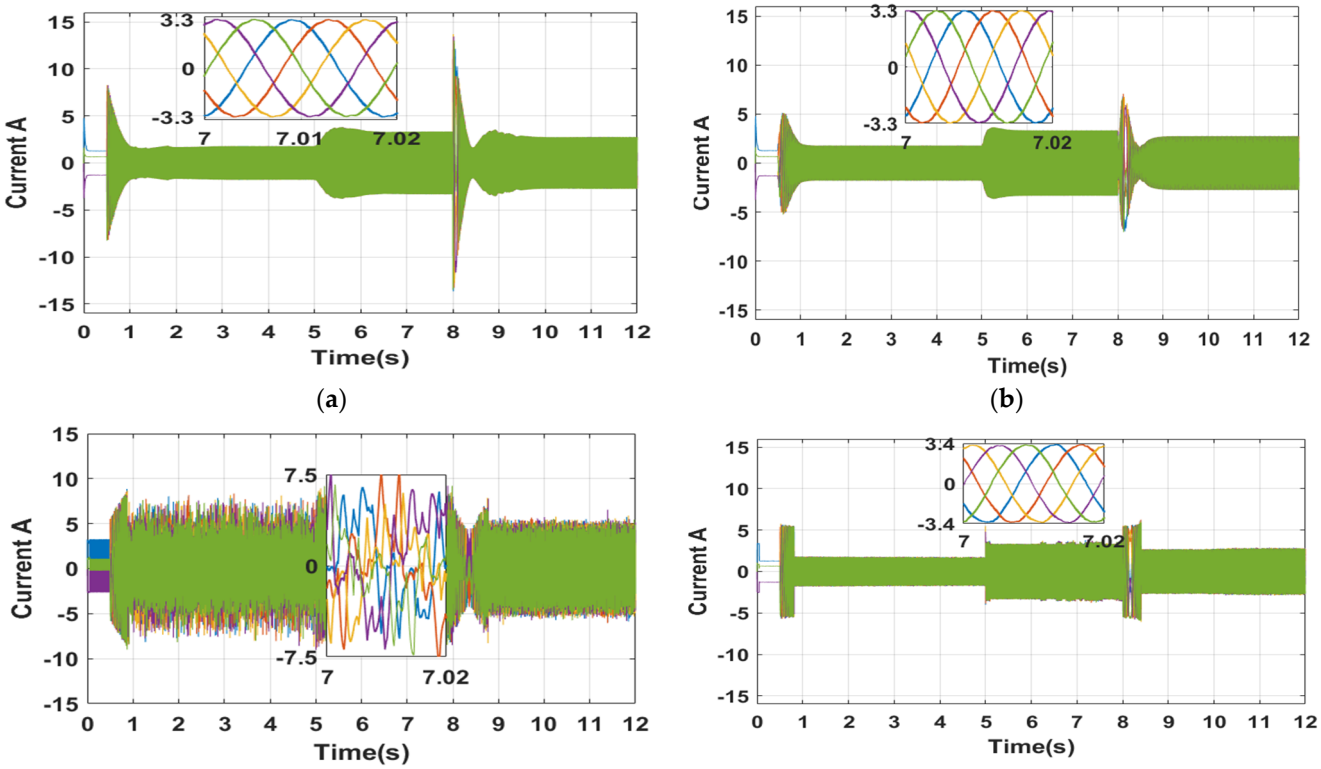

(**a**) (**b**)

(**c**) (**d**)

Figure 11. Five-phase stator current for DFOC based on: (**a**) PICs, (**b**) IPCs, (**c**) CSMCs, and (**d**) proposed SOSMC-STAs.

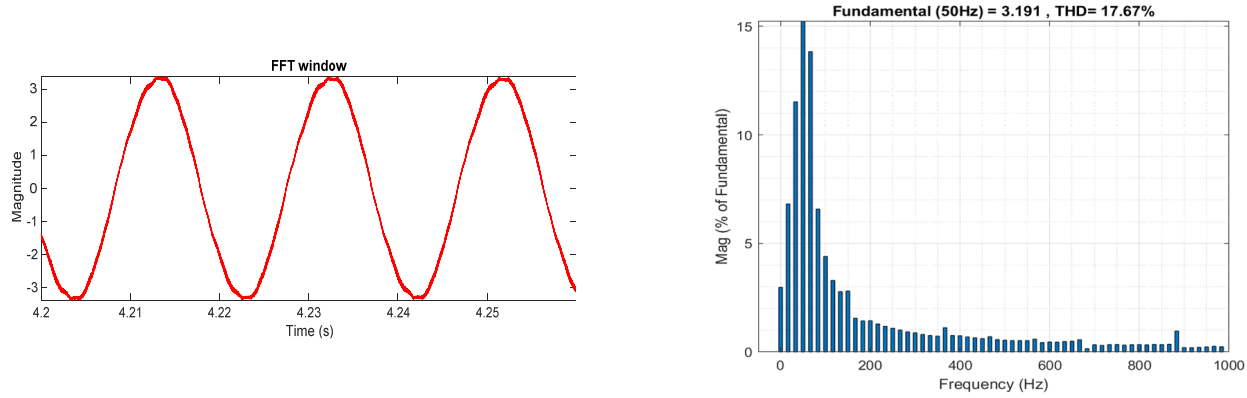

(**a**)

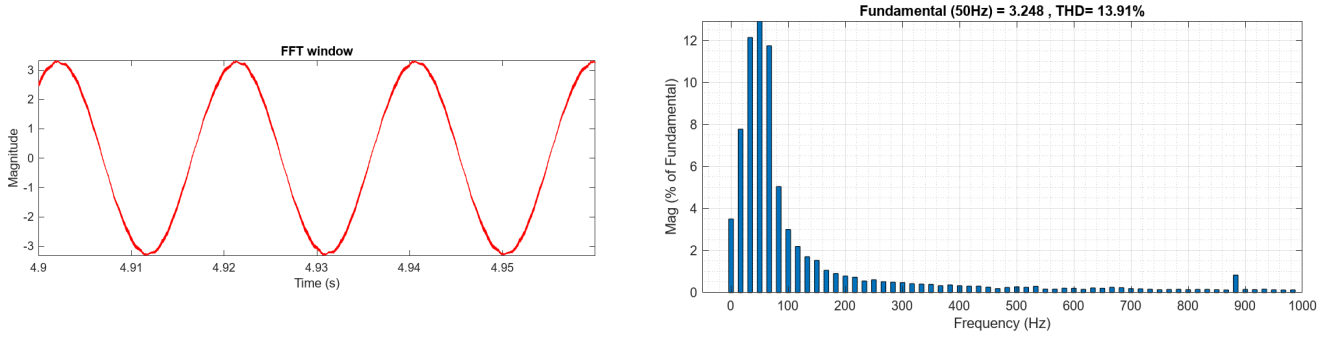

(**b**)

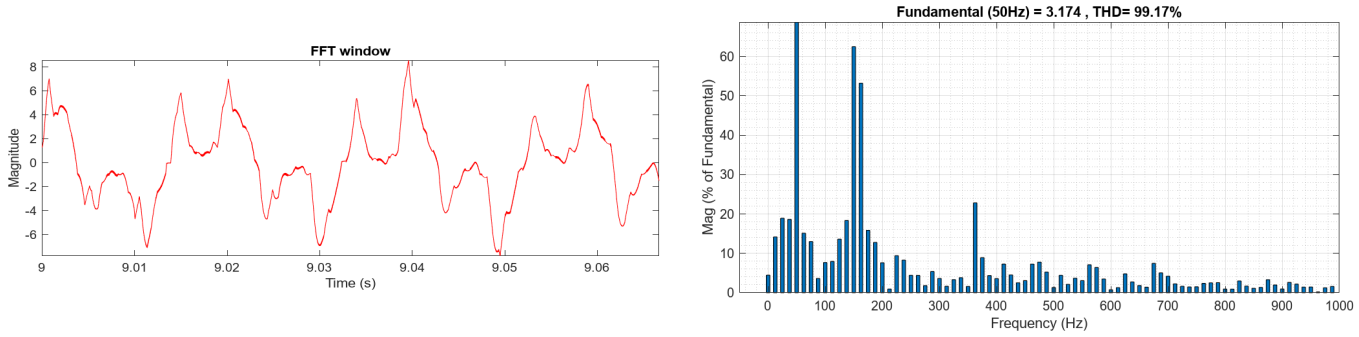

(**c**)

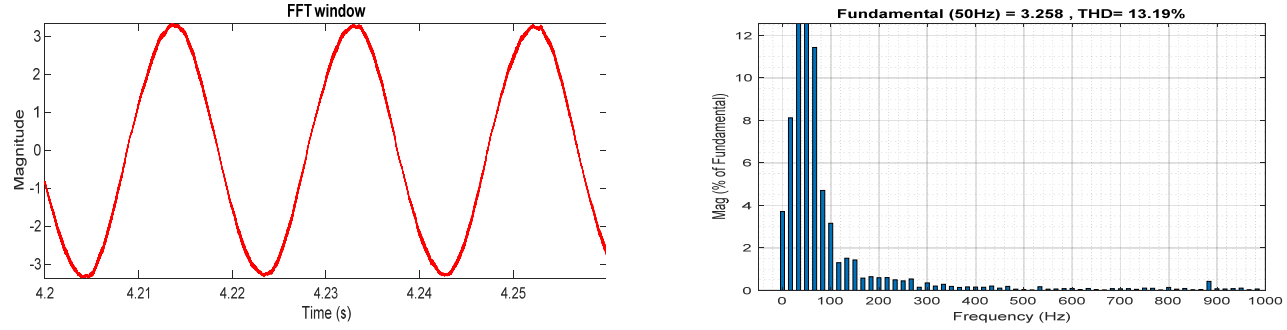

(**d**)

Figure 12. Spectral analysis of stator phase current "a" for the four types of controllers: (**a**) PICs, (**b**) IPCs, (**c**) CSMCs, and (**d**) proposed SOSMC-STAs.

Table 1. Comparison of different controllers (PICs, IPs, CSMCs, SOSMC-STAs) in outer speed loop.

Control Strategy	DFOC			
Criteria \ Controller	PICs	IPCs	CSMCs	Proposed SOSMC-STAs
Speed convergence time (s)	2	1	0.35	0.31
Drop in speed when load is applied (rad/s)	28.6	10.8	0.4	0.2
Chattering	Very low	Very low	0.085	Neglected
Speed response time after applying load (s)	1.3	0.85	0.005	0.003
Overshooting (rad/s)	30	0	0.2	Neglected
Torque ripples (%)	1.19	1.19	47.6	0.47
Torque response time when a load is applied (s)	2	1	neglected	Neglected
Current distortions	Slightly distorted	Slightly distorted	Heavily distorted	Slightly distorted
THD (%)	17.67	13.91	99.17	13.19

Figure 10 illustrates the evolution of the direct and quadratic stator current components i_{sd} and i_{sq}, and the rotor flux module. As depicted in Figure 10a,b, it can be seen that the direct stator current component and flux, and both the quadrature stator current and the torque, are proportional, which confirms that decoupling between the flux and the torque is effective. As shown in these figures, for CSMCs the current components i_{sd} and i_{sq} converge rapidly towards their reference values, but with high chattering. However, when the PICs and IPCs are employed, the chattering is attenuated, but a slow convergence in observed. It can be seen also that the suggested SOSMC-STAs provide excellent and better performance that combines rapid convergence and neglected chattering. Figure 10c shows the responses of the rotor flux when the FPIM is controlled with PICs, IPCs, SMCs, and our proposed SOSMC-STAs, respectively. For all controllers, the responses are fast, precise, and do not exhibit overshooting, except for the SMCs, which exhibit chattering phenomena in their response.

The simulation results presented in Figures 11 and 12 depict the five-phase stator currents of the FPIM under the control of the DFOC strategies based on PICs, IPCs, SMCs, and our proposed SOSMC-STAs, respectively. These results indicate that the SMCs generate stator currents with significant harmonics and relatively high amplitudes compared to the other tested controllers, which is deemed unacceptable in terms of harmonic presence.

8.2. Second Case: Performance Analysis of Suggested SOSMC-STAs at Low Speed

The objective of this scenario is to justify the better performance provided by the suggested SOSMC-STAs even at low-speed operations. In fact, in Figure 13, a simulation study of a gradual startup with a progressive direction reversal of the machine according to the speed reference profile given by the same figure is conducted. From 5 s until the end of the simulation, a constant load torque of 7.2 Nm is applied. It can be observed that the choice of PICs and IPCs is not appropriate, as the speed reaches negative values during the application of the load. On the other hand, the speed response shows a decrease of 0.12 rad/s and 0.09 rad/s, respectively, for SMCs and our suggested SOSMC-STAs, just at the moment of load applications. Then it follows its reference profile with ripples of 0.1 rad/s for SMCs and neglected ripples for the proposed SOSMC-STAs. The SMCs still exhibit a chattering phenomenon. For further clarification, a comparative study is provided in Table 2.

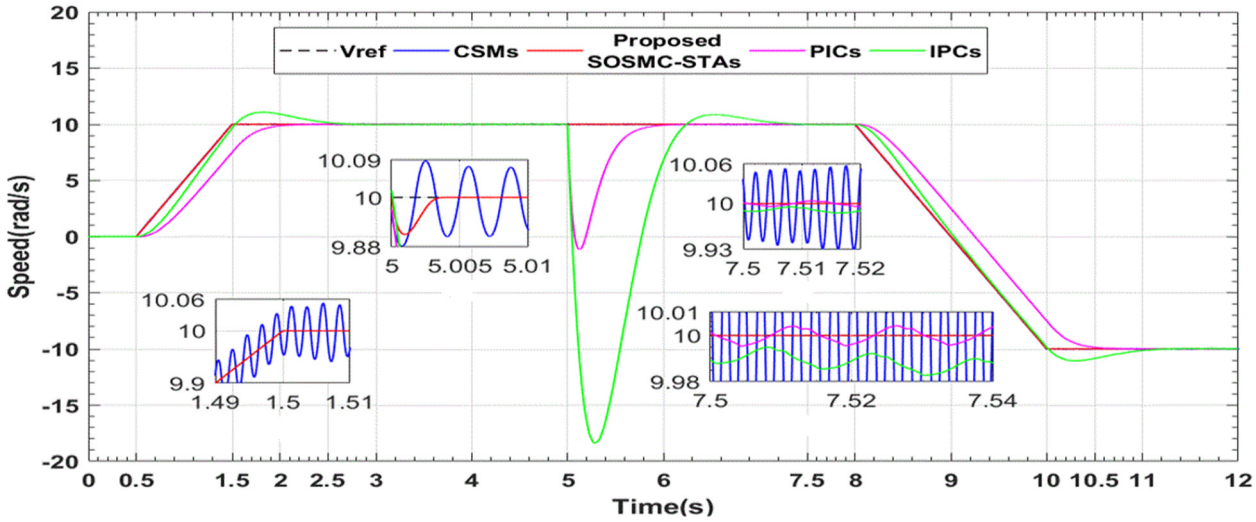

Figure 13. Low-speed response for RFOC based on PICs, IPCs, CSMCs, and the suggested SOSMC-STAs at low speed with gradual start and reversal of rotation.

Table 2. Performance analysis of proposed controller at low speed.

Control Strategy	DFOC			
Criteria \ Controller	PICs	IPCs	CSMCs	Proposed SOSMC-STA
Tracking Accuracy	Poor	Medium	Good	Excellent
Deviation when load is applied (rad/s)	10 to −18	10 to −0.9	10 to 9.88	10 to 9.9
Speed response time to reach 10	1	0.5	Neglected	Neglected
Speed response time to reach −10	1	0.5	Neglected	Neglected
Chattering (%)	0.05	0.05	0.3	Neglected
Decision	Not suitable	Not suitable	Not suitable	Suitable
ITAE	79.37	61.09	2.93	0.02
IAE	20.97	11.25	0.49	0.0004
ISE	364.1	44.66	0.03	1.8×10^{-5}

8.3. Robustness Study of Suggested SOSMC-STAs with Rotor Resistance Variation at Low Speed

This case is put forward in order to compare the robustness of PICs, IPCs, CSMCs, and our proposed SOSMC-STAs under stator resistance variations at low-speed operations. Indeed, the speed reference is maintained at 5 rad/s from 0.5 s until the end of the simulation. At t = 3 s, a load torque of 7.2 Nm is applied, and from t = 5.5 s to t = 7.7 s, the rotor resistance is increased to reach $1.75 \times R_{rn}$, as given in Figure 14a. From 10.5 s until the end of the simulation, the rotor resistance decreases to reach its nominal value R_{rn}. Figure 14b illustrates the low rotor speed response under resistance variations. It is observed that at the moment of the rotor resistance variation, whether it is 75% or −75%, the rotor speed exhibits a significant overshooting, reaching approximately 60% for PICs and 20% for IPCs. In contrast, for the CSMCs, the speed remains relatively close to the reference profile with oscillations of about 3% around it. As for the SOSMC-STAs, the speed follows the reference with negligible disturbances. These results confirm the robustness of the SOSMC-STAs. Figure 14c depicts the variation in the electromagnetic torque for the four different types of controllers being compared. One can observe that the employment of CSMCs exhibits rapid convergence towards the load torque and maintains robustness even when the rotor resistance varies. However, they introduce significant torque ripples. IPCs and PICs show slow convergence towards the load and additional oscillations when the rotor resistance changes. However, the suggested SOSMC-STA provides satisfactory performance in terms of ripple reduction, rapid convergence towards the reference, and excellent robustness

under rotor resistance variations. To provide additional clarity, a comparative analysis is presented in Table 3.

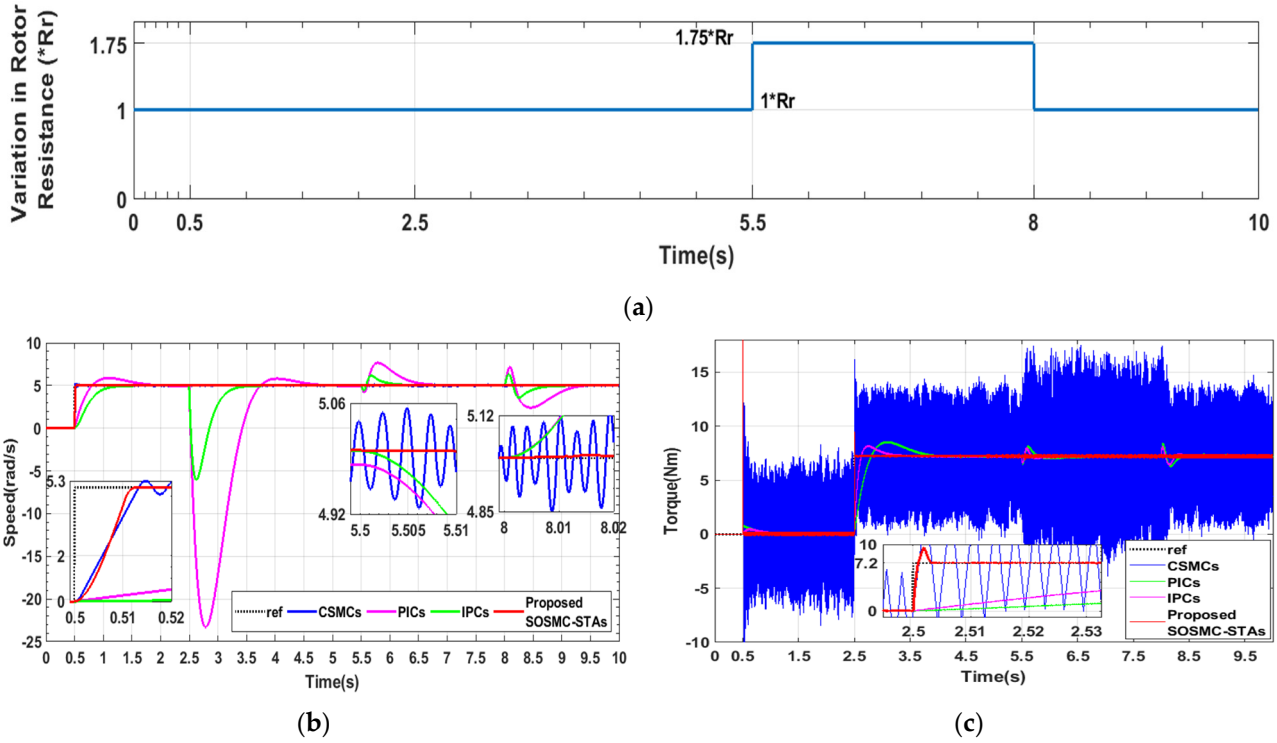

Figure 14. Low-speed response for the DFOC based on PICs, CSMCs, and SOSMC-STAs with variation in rotor resistance: (**a**) Profile of rotor resistance variation, (**b**) Speed response, (**c**) Electromagnetic torque response.

Table 3. Analysis of Proposed Controller at Low Speed.

Control Strategy	DFOC			
Controller / Criteria	PICs	IPCs	CSMCs	Proposed SOSMC-STA
Speed response time (s)	1.25	0.625	0.016	0.012
Speed overshoot (%)	1	0	Neglected	0
Speed deviation when R_r increases (rad/s)	5 to 4 to 8	5 to 4 to 6	Neglected	Neglected
Speed deviation when R_r decreases (rad/s)	5 to 7 to 2	5 to 6 to 3.5	Neglected	Neglected
Chattering (%)	Neglected	Neglected	3	Neglected
Robustness under R_r variation	Poor	Poor	Good	Excellent

8.4. Fourth Case: Loss Reduction and Efficiency Optimization

This scenario is proposed in order to test the performance of the suggested LMC mechanism-based DFOC with our SOSMC-STAs in terms of loss reduction and efficiency optimization. The reference speed is maintained at 150 rad/s starting from t = 0.5 s, while a load torque of 7.2 Nm is introduced at t = 3 s. The FPIM starts with a constant flux reference of 1 Wb, and at t = 4 s the LMC strategy is activated. The simulation results are illustrated in Figure 15, highlighting the total copper losses and the efficiency of the FPIM, respectively. These results confirm the effectiveness of integrating the LMC with the DFOC-SOSMC-STAs. Table 4 provides these comparison results in a numerical form.

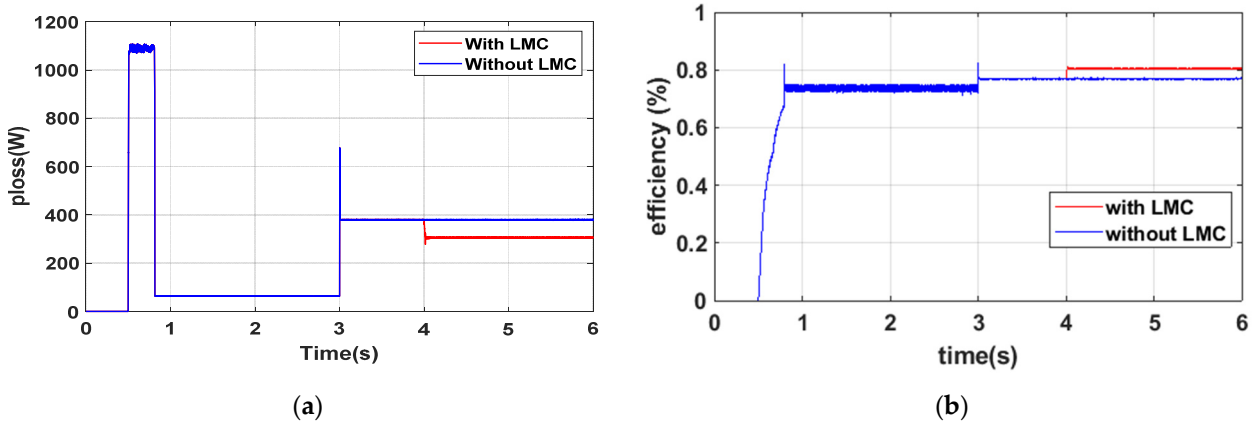

(**a**) (**b**)

Figure 15. (**a**) Total losses, (**b**) efficiency.

Table 4. Numerical Values from Simulation of LMC Integrated With DFOC-SOSMC-STAs.

Criteria	DFOC Based on Proposed SOSMC-STAs	
	Without LMC	With LMC
Power losses (W)	380	304.9
Efficiency (%)	76.85	80.5

9. Conclusions

In this paper, an improved DFOC based on new SOSMC-STAs and an LMC mechanism for an FPIM has been developed, designed, and simulated using the Matlab/Simulink environment. Hence, the key findings in this current study can be encapsulated as follows:

Firstly, for enhancing the speed, flux, quadratic, and direct current regulation loops, PICs and IPCs are replaced by new, robust SOSMC-STAs. The SOSMC-STAs are proposed in order to improve DFOC robustness under rotor resistance variations and sudden load torque applications. Moreover, the latter controller is also suggested for preventing the chattering phenomenon which exists when CSMCs are employed. A comparative study between four controllers, which are PICs, IPCs, CSMCs, and our proposed SOSMC-STA-based DFOC, is put forward. This comparison illustrates that, when combined with the DFOC strategy, the latter controllers deliver superior performance, characterized by faster speed and torque responses, minimized ripples, and robustness in the face of rotor resistance variations. Indeed, simulation has been conducted across various operating conditions, including rated loads and speeds, low-speed operations, and variations in rotor resistance.

Secondly, this paper introduces an LMC based on online loss minimization for the FPIM. It is developed and added to the architecture of the suggested DFOC based on the SOSMC-STAs with the aim of reducing electrical energy consumption under nominal operations. The performance of the control strategy based on the proposed LMC is verified through a simulation study. The obtained results of the proposed DFOC based on the SOSMC-STAs and the LMC are compared with the proposed DFOC based on SOSMC-STAs without LMC methods. These results recorded better performance in terms of lower losses and greater efficiency. In fact, when the LMC is employed the power losses and the efficiency are equal to 304.9 W and 80.5%, respectively, whereas, without the LMC, the aforementioned control method records efficiency and power losses of 76.85% and 380 W, respectively.

Nevertheless, the outcomes affirm that the DFOC strategy based on the STA and LMC technique formulated in this paper stands as an appealing and promising alternative for the high-performance control of multi-phase machines. Nonetheless, it is essential to acknowledge that each control method comes with its own advantages and limitations. Therefore, there are additional challenges that need to be addressed in our forthcoming research:

(i) The proposed control method will be subject to validation through experimentation on a test bench based on an FPIM, a five-leg voltage source inverter, and a dSPACE controller board.
(ii) We will incorporate into the optimization algorithm the experimental model of iron losses, which also depends on the rotor flux level. Consequently, we can determine the optimal rotor flux that minimizes the total active losses.
(iii) The extension of the recommended control algorithm may serve as a fault-tolerant control technique under certain fault conditions.

Author Contributions: Conceptualization, H.M. and S.K.; methodology, H.M., S.K. and M.F.M.; software, H.M., S.K. and H.K.; validation, H.M., S.K. and M.F.M.; formal analysis, S.K. and M.F.M.; investigation, H.M., S.K. and M.F.M.; re-sources, H.M., S.K. and M.F.M.; data curation, H.M. and S.K.; writing—original draft preparation, H.M. and S.K.; writing—review and editing, S.K., H.K. and M.M.; visualization, H.M., S.K., H.K., M.M. and M.F.M.; supervision, S.K., M.F.M. and M.M. All authors have read and agreed to the published version of the manuscript.

Funding: Open Access funding provided by the Qatar National Library. The publication is the result of the Qatar National Re-search Fund (QNRF) research grant.

Institutional Review Board Statement: Not applicable.

Informed Consent Statement: Not applicable.

Data Availability Statement: Data are contained within the article.

Conflicts of Interest: The authors declare no conflicts of interest.

Appendix A

Table A1. Parameters of FPIM.

Symbol	Value
Rs/Rr	10 Ω/6.3 Ω
$Ls/Lr/Lm$	0.46 H/0.46 H/0.42 H
L_{ls}/L_{lr}	0.04 H/0.04 H
$J/P/f$	0.03 Kg·m^2/2/0.008 N·m·s
T_{en}	8.33 N·m

Table A2. Parameters of the proposed SOSMC-STA controller and CSMC controller.

Controller Type	Parameters	Value
Suggested SOSMC-STA speed controller	λ_Ω	20
	β_Ω	0.02
SOSMC-STA rotor flux controller	$\lambda_{\psi r}$	40
	$\beta_{\psi r}$	0.02
SOSMC-STA d-axis current controller	λ_d	80
	β_d	0.02
SOSMC-STA q-axis current controller	λ_q	80
	β_q	0.02
CSMC flux controller	k_Ω	60
CSMC speed controller	$k_{\psi r}$	12
CSMC d-axis current controller	k_d	400
CSMC q-axis current controller	k_q	400

Table A2. *Cont.*

Controller Type	Parameters	Value
PI $d(q)$-axis current controller	$T_{i\Omega}$	0.005
	$K_{p\Omega}$	0.0033
PI $x(y)$-axis current controller	T_{ix}	0.002
	K_{px}	86
PI flux controller	$T_{i\varphi r}$	0.073
	$K_{p\varphi r}$	8.2
PI speed controller	$T_{i\Omega}$	0.12
	$K_{p\Omega}$	0.94
IP $d(q)$-axis current controller	k_i	0.036
	k_p	4795
IP $x(y)$-axis current controller	k_i	940
	k_p	47,000
IP flux controller	k_i	89.5
	k_p	3289
IP speed controller	k_i	0.75
	k_p	6.4

Table A3. The relationship between ξ and ω_0 tresp.

Symbol	ξ	$w_0 \times tresp$
	0.4	7.7
	0.5	5.3
	0.6	5.2
	0.7	3
	1	4.75

References

1. Riveros, J.A.; Barrero, F.; Levi, E.; Duran, M.J.; Toral, S.; Jones, M. Variable-speed five-phase induction motor drive based on predictive torque control. *IEEE Trans. Ind. Electron.* **2012**, *60*, 2957–2968. [CrossRef]
2. Levi, E.; Bojoi, R.; Profumo, F.; Toliyat, H.; Williamson, S. Multiphase induction motor drives—A technology status review. *IET Electr. Power Appl.* **2007**, *1*, 489–516. [CrossRef]
3. Kulandaivel, G.; Sundaram, E.; Gunasekaran, M.; Chenniappan, S. Five-Phase induction Motor Drive-A Comprehensive Review. *Front. Energy Res.* **2023**, *11*, 1178169. [CrossRef]
4. Listwan, J.; Pieńkowski, K. Comparative analysis of control methods with model reference adaptive system estimators of a seven-phase induction motor with encoder failure. *Energies* **2021**, *14*, 1147. [CrossRef]
5. Mossa, M.A.; Echeikh, H.; El Ouanjli, N.; Alhelou, H.H. On this page. *Int. Trans. Electr. Energy Syst.* **2022**, *2*, 3.
6. Mossa, M.A.; Echeikh, H. A novel fault tolerant control approach based on backstepping controller for a five *phase* induction motor drive: Experimental investigation. *ISA Trans.* **2020**, *112*, 373–385. [CrossRef]
7. Bermudez, M.; Guzman, H.; Gonzalez-Prieto, I.; Barrero, F.; Duran, M.; Kestelyn, X. Comparative study of DTC and RFOC methods for the open-phase fault operation of a 5-phase induction motor drive. In Proceedings of the IECON 2015—41st Annual Conference of the IEEE Industrial Electronics Society, Yokohama, Japan, 9–12 November 2015; pp. 002702–002707.
8. Wolbank, T.; Moucka, A.; Machl, J. A comparative study of field-oriented and direct-torque control of induction motors reference to shaft-sensorless control at low and zero-speed. In Proceedings of the IEEE Internatinal Symposium on Intelligent Contro, Vancouver, BC, Canada, 30 October 2002; pp. 391–396.
9. Idris, N.; Yatim, A. Direct torque control of induction machines with constant switching frequency and reduced torque ripple. *IEEE Trans. Ind. Electron.* **2004**, *51*, 758–767. [CrossRef]
10. Krim, S.; Gdaim, S.; Mtibaa, A.; Mimouni, M.F. Control with high performances based DTC strategy: FPGA implementation and experimental validation. *EPE J.* **2018**, *29*, 82–98. [CrossRef]
11. Krim, S.; Gdaim, S.; Mtibaa, A.; Mimouni, M.F. Contribution of the FPGAS for complex control algorithms: Sensorless dtfc with an ekf of an induction motor. *Int. J. Autom. Comput.* **2016**, *16*, 226–237. [CrossRef]

12. Casadei, D.; Profumo, F.; Serra, G.; Tani, A. FOC and DTC: Two viable schemes for induction motors torque control. *IEEE Trans. Power Electron.* **2002**, *17*, 779–787. [CrossRef]
13. Liu, X.; Yu, H.; Yu, J.; Zhao, L. Combined speed and current terminal sliding mode control with nonlinear disturbance observer for pmsm drive. *IEEE Access* **2018**, *6*, 29594–29601. [CrossRef]
14. Krim, S.; Gdaim, S.; Mimouni, M.F. Robust direct torque control with super-twisting sliding mode control for an induction motor drive. *Complexity* **2019**, *2019*, 7274353. [CrossRef]
15. Rubio, J.D.J.; Orozco, E.; Cordova, D.A.; Islas, M.A.; Pacheco, J.; Gutierrez, G.J.; Zacarias, A.; Soriano, L.A.; Meda-Campana, J.A.; Mujica-Vargas, D. Modified linear technique for the controllability and observability of robotic arms. *IEEE Access* **2022**, *10*, 3366–3377. [CrossRef]
16. Rubio, J.D.J. Bat algorithm based control to decrease the control energy consumption and modified bat algorithm based control to increase the trajectory tracking accuracy in robots. *Neural Netw.* **2023**, *161*, 437–448. [CrossRef] [PubMed]
17. Lughofer, E.; Skrjanc, I. Evolving error feedback fuzzy model for improved robustness under measurement noise. *IEEE Trans. Fuzzy Syst.* **2022**, *31*, 997–1008. [CrossRef]
18. Bouguenna, I.F.; Tahour, A.; Kennel, R.; Abdelrahem, M. Multiple-vector model predictive control with fuzzy logic for pmsm electric drive systems. *Energies* **2021**, *14*, 1727. [CrossRef]
19. Hermassi, M.; Krim, S.; Kraiem, Y.; Hajjaji, M.A.; Alshammari, B.M.; Alsaif, H.; Alshammari, A.S.; Guesmi, T. Design of Vector Control Strategies Based on Fuzzy Gain Scheduling PID Controllers for a Grid-Connected Wind Energy Conversion System: Hardware FPGA-in-the-Loop Verification. *Electronics* **2023**, *12*, 1419. [CrossRef]
20. Lim, C.S.; Levi, E.; Jones, M.; Rahim, N.A.; Hew, W.P. FCS-MPC-based current control of a five-phase induction motor and its comparison with pi-pwm control. *IEEE Trans. Ind. Electron.* **2013**, *61*, 149–163. [CrossRef]
21. Martin, C.; Arahal, M.R.; Barrero, F.; Duran, M.J. Five-phase induction motor rotor current observer for finite control set model predictive control of stator current. *IEEE Trans. Ind. Electron.* **2016**, *63*, 4527–4538. [CrossRef]
22. Chihi, A.; Ben Azza, H.; Jemli, M.; Sellami, A. Nonlinear integral sliding mode control design of photovoltaic pumping system: Real time implementation. *ISA Trans.* **2017**, *70*, 475–485. [CrossRef]
23. Sami, I.; Ullah, S.; Basit, A.; Ullah, N.; Ro, J.-S. Integral super twisting sliding mode based sensorless predictive torque control of induction motor. *IEEE Access* **2020**, *8*, 186740–186755. [CrossRef]
24. Laoufi, C.; Sadoune, Z.; Abbou, A.; Akherraz, M. New model of electric traction drive based sliding mode controller in field-oriented control of induction motor fed by multilevel inverter. *Int. J. Power Electron. Drive Syst. (IJPEDS)* **2020**, *11*, 242. [CrossRef]
25. Krim, S.; Gdaim, S.; Mtibaa, A.; Mimouni, M.F. Real time implementation of DTC based on sliding mode speed controller of an induction motor. In Proceedings of the 2015 16th International Conference on Sciences and Techniques of Automatic Control and Computer Engineering (STA), Monastir, Tunisia, 21–23 December 2015; pp. 94–100.
26. Silva-Ortigoza, R.; Hernández-Márquez, E.; Roldán-Caballero, A.; Tavera-Mosqueda, S.; Marciano-Melchor, M.; Garcia-Sanchez, J.R.; Hernández-Guzmán, V.M.; Silva-Ortigoza, G. Sensorless tracking control for a "full-bridge Buck inverter–DC motor" system: Passivity and flatness-based design. *IEEE Access* **2021**, *9*, 132191–132204. [CrossRef]
27. Soriano, L.A.; Zamora, E.; Vazquez-Nicolas, J.M.; Hernández, G.; Madrigal, J.A.B.; Balderas, D. PD control compensation based on a cascade neural network applied to a robot manipulator. *Front. Neurorobotics* **2020**, *14*, 577749. [CrossRef] [PubMed]
28. Krim, Y.; Abbes, D.; Krim, S.; Mimouni, M.F. Power management and second-order sliding mode control for standalone hybrid wind energy with battery energy storage system. *Proc. Inst. Mech. Eng. Part I J. Syst. Control. Eng.* **2018**, *232*, 1389–1411. [CrossRef]
29. Utkin, V.; Guldner, J.; Shi, J. *Sliding Mode Control in Electro-Mechanical Systems*; CRC Press: Boca Raton, FL, USA, 2009. [CrossRef]
30. Krim, Y.; Abbes, D.; Krim, S.; Mimouni, M.F. A second-order sliding-mode control for a real time emulator of a wind power system synchronized with electrical network. *Int. Trans. Electr. Energy Syst.* **2019**, *29*, e12051. [CrossRef]
31. Bendjeddou, Y.; Deboucha, A.; Bentouhami, L.; Merabet, E.; Abdessemed, R. Super twisting sliding mode approach applied to voltage orientated control of a stand-alone induction generator. *Prot. Control. Mod. Power Syst.* **2021**, *6*, 18. [CrossRef]
32. Utkin, V.; Shi, J. Integral sliding mode in systems operating under uncertainty conditions. In Proceedings of the 35th IEEE Conference on Decision and Control, Kobe, Japan, 13 December 1996; Volume 4, pp. 4591–4596.
33. Krim, S.; Krim, Y.; Mimouni, M.F. Sensorless direct torque control based on nonlinear integral sliding mode controllers for an induction motor drive: Experimental verification. *Proc. Inst. Mech. Eng. Part I J. Syst. Control. Eng.* **2020**, *235*, 249–268. [CrossRef]
34. Burton, J.A.; Zinober, A.S.I. Continuous approximation of variable structure control. *Int. J. Syst. Sci.* **1986**, *17*, 875–885. [CrossRef]
35. Boiko, I.M. Chattering in sliding mode control systems with boundary layer approximation of discontinuous control. *Int. J. Syst. Sci.* **2013**, *44*, 1126–1133. [CrossRef]
36. Plestan, F.; Shtessel, Y.; Brégeault, V.; Poznyak, A. New methodologies for adaptive sliding mode control. *Int. J. Control* **2010**, *83*, 1907–1919. [CrossRef]
37. Zhang, J.; Shi, P.; Xia, Y. Robust adaptive sliding-mode control for fuzzy systems with mismatched uncertainties. *IEEE Trans. Fuzzy Syst.* **2010**, *18*, 700–711. [CrossRef]
38. Tang, Y.; Zhang, X.; Zhang, D.; Zhao, G.; Guan, X. Fractional order sliding mode controller design for antilock braking systems. *Neurocomputing* **2013**, *111*, 122–130. [CrossRef]
39. Delavari, H.; Ghaderi, R.; Ranjbar, A.; Momani, S. Fuzzy fractional order sliding mode controller for nonlinear systems. *Commun. Nonlinear Sci. Numer. Simul.* **2010**, *15*, 963–978. [CrossRef]

40. Fayazi, A.; Rafsanjani, H.N. Fractional order fuzzy sliding mode controller for robotic flexible joint manipulators. In Proceedings of the 2011 9th IEEE International Conference on Control and Automation (ICCA 2011), Santiago, Chile, 19–21 December 2011; pp. 1244–1249.
41. Zhang, B.; Pi, Y.; Luo, Y. Fractional order sliding-mode control based on parameters auto-tuning for velocity control of permanent magnet synchronous motor. *ISA Trans.* **2012**, *51*, 649–656. [CrossRef]
42. Cao, D.; Fei, J. Adaptive fractional fuzzy sliding mode control for three-phase active power filter. *IEEE Access* **2016**, *4*, 6645–6651. [CrossRef]
43. Efe, M.Ö. Fractional order sliding mode control with reaching law approach. *Turk. J. Electr. Eng. Comput. Sci.* **2010**, *18*, 731–748. [CrossRef]
44. Zaihidee, F.M.; Mekhilef, S.; Mubin, M. Application of fractional order sliding mode control for speed control of permanent magnet synchronous motor. *IEEE Access* **2019**, *7*, 101765–101774. [CrossRef]
45. Fei, J.; Lu, C. Adaptive fractional order sliding mode controller with neural estimator. *J. Frankl. Inst.* **2018**, *355*, 2369–2391. [CrossRef]
46. Rubio, J.d.J.; Hernandez, M.A.; Rosas, F.J.; Orozco, E.; Balcazar, R.; Pacheco, J. Genetic high-gain controller to improve the position perturbation attenuation and compact high-gain controller to improve the velocity perturbation attenuation in inverted pendulums. *Neural Netw.* **2023**, *170*, 32–45. [CrossRef]
47. Levant, A. Higher-order sliding modes, differentiation and output-feedback control. *Int. J. Control.* **2003**, *76*, 924–941. [CrossRef]
48. Chen, Q.; Li, C. Super-twisting algorithm for second-order sliding mode control. In Proceedings of the 2021 China Automation Congress (CAC), Beijing, China, 22–24 October 2021; pp. 1836–1840.
49. Ammar, A.; Benakcha, A.; Bourek, A. Closed loop torque SVM-DTC based on robust super twisting speed controller for induction motor drive with efficiency optimization. *Int. J. Hydrogen Energy* **2017**, *42*, 17940–17952. [CrossRef]
50. Listwan, J. Application of super-twisting sliding mode controllers in direct field-oriented control system of six-phase induction motor: Experimental studies. *Power Electron. Drives* **2018**, *3*, 23–34. [CrossRef]
51. Li, J.; Xu, L.; Zhang, Z. A new efficiency optimization method on vector control of induction motors. In Proceedings of the IEEE International Conference on Electric Machines and Drives, San Antonio, TX, USA, 15 May 2005; pp. 1995–2001.
52. Listwan, J.; Pienkowski, K. Control of five-phase induction motor with application of second-order sliding-mode Direct Field-Oriented method. In Proceedings of the 2017 International Symposium on Electrical Machines (SME), Naleczow, Poland, 18–21 June 2017; pp. 1–6.
53. Kali, Y.; Rodas, J.; Saad, M.; Gregor, R.; Benjielloun, K.; Doval-Gandoy, J.; Goodwin, G. Speed control of a five-phase induction motor drive using modified super-twisting algorithm. In Proceedings of the 2018 International Symposium on Power Electronics, Electrical Drives, Automation and Motion (SPEEDAM), Amalfi, Italy, 20–22 June 2018; pp. 938–943.
54. de Almeida Souza, D.; de Aragao Filho, W.C.; Sousa, G.C.D. Adaptive fuzzy controller for efficiency optimization of induction motors. *IEEE Trans. Ind. Electron.* **2007**, *54*, 2157–2164. [CrossRef]
55. Raj, C.T.; Srivastava, S.P.; Agarwal, P. Differential Evolution based Optimal Control of Induction Motor Serving to Textile Industry. *IAENG Int. J. Comput. Sci.* **2008**, *35*, IJCS_35_2_03.
56. Abrahamsen, F.; Blaabjerg, F.; Pedersen, J.; Grabowski, P.; Thogersen, P. On the energy optimized control of standard and high-efficiency induction motors in CT and HVAC applications. *IEEE Trans. Ind. Appl.* **1998**, *34*, 822–831. [CrossRef]
57. Moreno, J.; Cipolla, M.; Peracaula, J.; Branco, P.D.C. Fuzzy logic based improvements in efficiency optimization of induction motor drives. In Proceedings of the 6th International Fuzzy Systems Conference, Barcelona, Spain, 5 July 1997; Volume 1, pp. 219–224.
58. Bose, B.; Patel, N.; Rajashekara, K. A neuro-fuzzy-based on-line efficiency optimization control of a stator flux-oriented direct vector-controlled induction motor drive. *IEEE Trans. Ind. Electron.* **1997**, *44*, 270–273. [CrossRef]
59. Uddin, M.N.; Nam, S.W. New online loss-minimization-based control of an induction motor drive. *IEEE Trans. Power Electron.* **2008**, *23*, 926–933. [CrossRef]
60. Aher, K.S.; Thosar, A.G. Modeling and simulation of five phase induction motor using MATLAB/simulink. *Int. J. Eng. Res. Appl.* **2016**, *6*, 1–8.
61. Iqbal, A.; Levi, E. Space vector modulation schemes for a five-phase voltage source inverter. In Proceedings of the 2005 IEEE 11th European Conference on Power Electronics and Applications, Dresden, Germany, 11–14 September 2005; p. 12.
62. Razafinjaka, J.N.; Patrick, A.T. Comparaison Des Performances Des Regulateurs Pi Et Ip Appliques Aux Systemes Fondamentaux. *Res. Inc. Fév.* 2015. Available online: https://www.researchgate.net/publication/272748849_COMPARAISON_DES_PERFORMANCES_DES_REGULATEURS_PI_ET_IP_APPLIQUES_AUX_SYSTEMES_FONDAMENTAUX (accessed on 4 December 2023).
63. Ajmi, A.; Krim, S.; Hosseyni, A.; Mansouri, M.; Mimouni, M.F. Robust Variable Structure Control Approach of Two Series-Connected Five-Phase PMSMs Under Healthy and Faulty Operation Modes. *IEEE Access* **2023**, *11*, 96401–96422. [CrossRef]
64. Young, K.D.; Utkin, V.I.; Ozguner, U. A control engineer's guide to sliding mode control. *IEEE Trans. Control. Syst. Technol.* **1999**, *7*, 328–342. [CrossRef]
65. Utkin, V.I. Sliding mode control design principles and applications to electric drives. *IEEE Trans. Ind. Electron.* **1993**, *40*, 23–36. [CrossRef]
66. Lee, J.; Jeong, S. Robust Temperature Control of a Variable-Speed Refrigeration System Based on Sliding Mode Control with Optimal Parameters Derived Using the Genetic Algorithm. *Energies* **2021**, *14*, 6321. [CrossRef]

67. Ahmed, S.; Adil, H.M.M.; Ahmad, I.; Azeem, M.K.; e Huma, Z.; Khan, S.A. Supertwisting sliding mode algorithm based nonlinear mppt control for a solar pv system with artificial neural networks based reference generation. *Energies* **2020**, *13*, 3695. [CrossRef]
68. Rashed, M.; Goh, K.; Dunnigan, M.; MacConnell, P.; Stronach, A.; Williams, B. Sensorless second-order sliding-mode speed control of a voltage-fed induction-motor drive using nonlinear state feedback. *IEE Proc. Electr. Power Appl.* **2005**, *152*, 1127. [CrossRef]
69. Lascu, C.; Boldea, I.; Blaabjerg, F. Super-twisting sliding mode control of torque and flux in permanent magnet synchronous machine drives. In Proceedings of the IECON 2013—39th Annual Conference of the IEEE Industrial Electronics Society, Vienna, Austria, 10–13 November 2013; pp. 3171–3176.
70. Boubzizi, S.; Abid, H.; El Hajjaji, A.; Chaabane, M. Comparative study of three types of controllers for DFIG in wind energy conversion system. *Prot. Control. Mod. Power Syst.* **2018**, *3*, 21. [CrossRef]
71. Moreno, J.A.; Osorio, M. A Lyapunov approach to second-order sliding mode controllers and observers. In Proceedings of the 2008 47th IEEE Conference on Decision and Control, Cancun, Mexico, 9–11 December 2008; pp. 2856–2861. [CrossRef]
72. Liu, Y.-C.; Laghrouche, S.; Depernet, D.; N'Diaye, A.; Djerdir, A.; Cirrincione, M. Super-twisting sliding-mode observer-based model reference adaptive speed control for PMSM drives. *J. Frankl. Inst.* **2023**, *360*, 985–1004. [CrossRef]
73. Dávila, A.; Moreno, J.A.; Fridman, L. Optimal Lyapunov function selection for reaching time estimation of super twisting algorithm. In Proceedings of the 48h IEEE Conference on Decision and Control (CDC) held jointly with 2009 28th Chinese Control Conference, Shanghai, China, 15–18 December 2009; pp. 8405–8410.
74. Feng, Z.; Fei, J. Design and analysis of adaptive Super-Twisting sliding mode control for a microgyroscope. *PLoS ONE* **2018**, *13*, e0189457. [CrossRef] [PubMed]